Fermilab

SSC DETECTOR SOLENOID DESIGN NOTE #110

TITLE: An Air-Core Solenoidal Detector (ACS) for High Pt Physics at the SSC

AUTHOR: T. Kondo, KEK, Japan

DATE: Mar 13, 1990

ABSTRACT: This Design Note consists of a write-up of Kondo's talk given at the Fermilab Workshop on Solenoidal Detector for the SSC, Sept 25-26, 1989. It is referenced as JSD-NOTE-1990-5, dated Jan 20, 1990.

JSD-NOTE-1990-5

An Air-Core Solenoidal Detector (ACS) for High P_t Physics at the SSC *

January 20, 1990

ACS study group

presented by T.Kondo (KEK)

* Talk given at the Fermilab Workshop on Solenoidal Detector for the SSC, September 25-26, 1989.

Contents

Abstract 3
1. Introduction 3
2. Requirements to the detector 4
3. Design considerations ..... 3.1 Coil location 5
3.2 Long coil versus short coil 6
3.3 Need for muon toroids 8
3.4 Choice of calorimeter technology 9
3.5 Hybrid tracking system 10
4. Structural considerations 10
5. Superconducting solenoid ..... 5.1 Coil thickness 16
5.2 Design of superconducting solenoid 17
5.3 Magnetic field profile 20
5.4 Forces on the coil 20
5.5 Quench simulation 23
6. Muon detector ..... 6.1 Detection of $H \rightarrow 4\mu$ 26
6.2 Muon hit rate and triggering 26
6.3 Design of muon toroid system 28
6.4 Muon momentum resolution 32
6.5 Muon chambers 38
7. Liquid Argon Calorimeter ..... 7.1 Why liquid argon ? 38
7.2 Experience with VENUS LAr detector 39
7.3 Wave form simulation 42
7.4 The e/h ratio 42
7.5 Preamplifiers in the liquid 49
8. Inner Tracking System ..... 8.1 Hit rate 51
8.2 Wave form simulation 51
8.3 Hybrid tracker system 54
8.4 Straw tube system 55
8.5 Silicon strip detectors 59
8.6 Momentum resolution 60
8.7 Non-uniform magnetic field 60
8.8 TMC 60
8.9 On-chip filtering of low p_t tracks 66
9. Conclusions 66
Acknowledgements 67
References and Notes 68

ABSTRACT

An outline of a general purpose 4π detector for high p_t physics at the SSC is described. The detector uses a thin air-core solenoid inside the calorimeter. Related design and simulation results are presented with an emphasis on structural aspects.

1. Introduction

A general purpose 4π magnetic detector that works for pp collisions at $\sqrt{s}$=40 TeV and $L=10^{33}$ $cm^{-2}s^{-1}$ is proposed for the SSC. The present detector model, with a coil inside a liquid argon calorimeter, is based on the original detector idea presented by K.Ogawa(KEK) in one of SSC workshops held in Japan in 1988[1]. The present note summarizes the design essence as well as some results of our design studies followed by interested physicists since then[2]. In this note we focus our consideration on structural aspects of the detector, such as solenoid and muon toroids, and some of study results on detector components are included.

Our model detector is designed to aim optimization on (1) detection of high p_t muons and isolated electrons, (2) measurement of missing transverse energies, (3) identification of high p_t W and Z bosons as well as (4) system engineering aspects for reliable detector operation. As a consequence, the design puts high priorities on hermetic calorimetry, inner tracking, and muon detection system. Detector technologies employed are conservative enough to be realistic with a reasonable extrapolation of the present detector technology.

2. Requirements to the detector

The primary goal of this experiment is to explore the mechanism of the spontaneously symmetry breakdown as well as new physics beyond the standard model by studying high P_t phenomena in the TeV energy region. Major physics processes under consideration are

1. Heavy Higgs hunting,
2. WW scattering in $M_{WW} > 1$TeV,
2. New gauge boson search,
3. Compositeness scale study,
4. SUSY particle search,
5. QCD study,
6. New quark and lepton search.

Requirements to detectors for physics processes have been studied in various past workshops. Although there is no final consensus in detector requirements, followings represent "average and minimum" requirements from these studies [1,3];

EM energy resolution	$0.15/\sqrt{E} + 0.01$
hadronic energy resolution	$0.50/\sqrt{E} + 0.02$
transverse segmentation	$0.03 \sim 0.05$ in η and ϕ
fine calorimetry coverage	$\lvert y \rvert < 3$
coverage for missing E_t	$\lvert y \rvert < 5$
tracking resolution	$0.5\ P_t$(TeV)
electron (isolated) identification	> 20 GeV/c
e/π separation	10^{-3}
muon momentum resolution	$< 0.5\ P_t$ (TeV).

In addition, there are number of requirements on detectors to be fulfilled to accommodate the high rate/high radiation-level environment at the SSC[4]. Among others, detector elements must survive for at least 10 years of operation and thus be highly radiation resistant and stable.

It is worth to list the reasons why the presence of magnetic field in the inner tracking region is recommended[5] :

1. Electron charge
2. Improved and redundant muon momentum resolution
3. Redundant energy measurement
4. Credibility and flexibility for new physics and unusual topology
5. Secondary vertices
6. τ identification
7. Invariant mass
8. Pt of tracks and jet fragmentation
9. Electron identification (E/p)
10. Correction for cracks and dead channels
11. Calorimeter calibration
12. High P_t triggering and on-line filtering.

The list is in approximate order of priorities. We believe that the magnetic field with proper tracking devices greatly help in exploring new physics as well as understanding the signals and backgrounds more quantitatively.

3. Design Considerations

3.1 Coil location

The present design is based on the Large Solenoid Detector proposed at the Berkeley workshop in 1987[6], except for one important point, the location of the superconducting solenoid. The large solenoid might be too large to be a realistic component of the detector. Though the large solenoid can be built with an extrapolation of the existing technology, its design and construction as well as transportation and installation are non-trivial. For example, the quench protection for the stored energy of 1.6 GJ is one of non-trivial issues. It will take more than five years for construction[7]. Its diameter of 9.5m and the length of

16m may generate severe problems in its transportation[8]. The supporting mechanism including installation of the entire calorimeter (~3000 tons) inside the magnet cryostat will be an engineering challenge. As a consequence, it becomes clear that the large solenoid with associated calorimeter support is a major burden of the detector cost and the engineering efforts. It is worth reconsidering the effectiveness of the large solenoid together with its alternatives.

The main motivation of the large solenoid was to maintain good hermeticity by locating the entire central and endcap calorimeters inside the solenoid. By making the inner solenoid thin, the effect of a coil inside the calorimeter to hermeticity and energy measurement can be made effectively negligible. E.Wang demonstrated in his simulation, as shown in Fig.1, that the presence of coil with thickness of $2X_0$ in front of calorimeter give little effects on missing P_t spectrum[9]. The effect on electron identification is expected to be small if the radiation thickness of the coil is kept at around $1X_0$.

Recent progress in thin superconducting magnet technology and construction experiences cumulated at various colliders made it very practical to proceed a realistic design of 2 Tesla solenoid with radiation thickness comparable with existing thin solenoids, namely about $1X_0$[10]. It is likely that three years are enough for construction of a small superconducting magnet, and therefore plenty of lead time will be available for design and R&D coils. Other advantages of a small coil are easy transportation, less costly, less stringent requirements for support and cabling for calorimeter, a full testing capability at the factory.

3.2 Long coil versus short coil

In the design of coil inside, there are in principle two different choices of magnet configuration in conjunction with the calorimeter as shown in Fig.2. We call these two types of magnets, type-L and type-S. The type-L solenoid

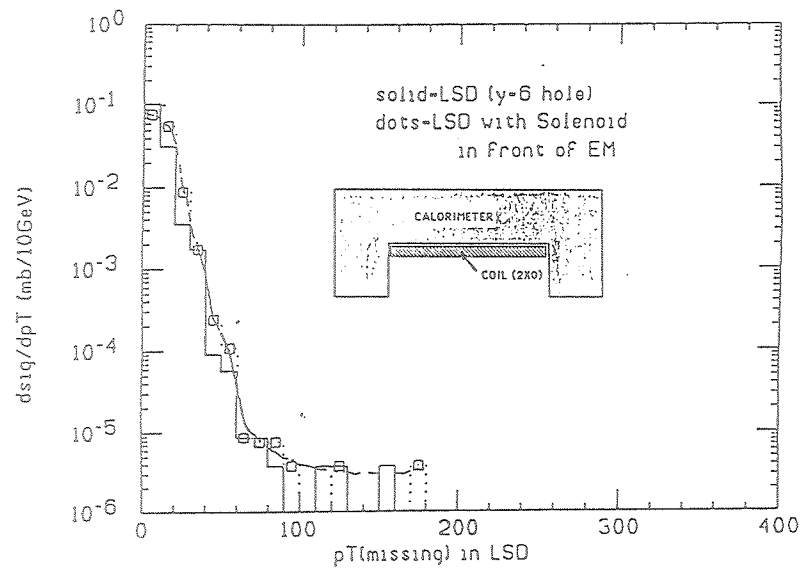

Fig.1 Missing Pt spectrum calculated by E.Wang[9]. The solid histogram is without solenoid and dots are with solenoid in front of EM calorimeter.

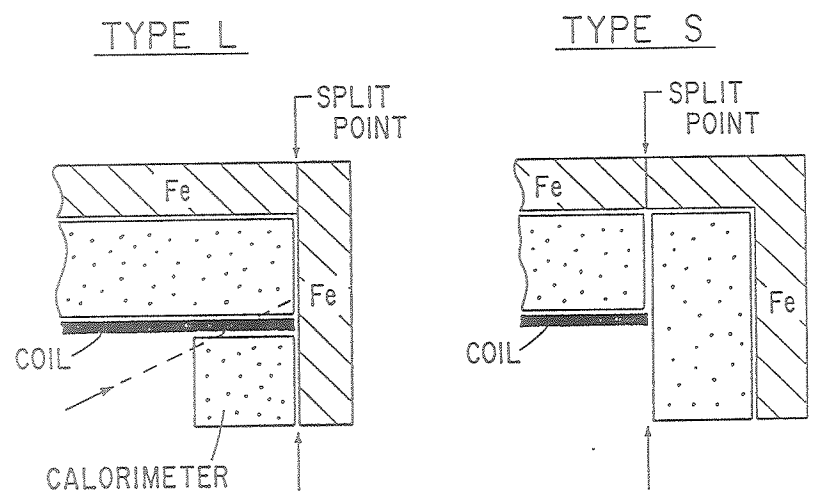

Fig.2 Two calorimeter configurations, Type L in the left and S in the right.

extends its coil to the iron flux return, while the type-S is a so-call air-core (iron free) magnet. We can point out advantages and disadvantages of each of magnet type qualitatively;

	type L	type S
B in tracking region	uniform	non-uniform
B in barrel region	field free	stray field present
B in forward region	full field	weaker field
calorimeter hermeticity	worse	better
force on forward yokes	large	very small
axial force on coil	small	large
decentering forces on coil	large	small

However, it is not easy to make a quantitative comparison between two configurations. It requires substantial simulation studies. We believe that both types of magnets can be built. Some technical details on the type S solenoid are described later. We take the hermeticity requirement for calorimetry more important than the non-uniform field in the inner tracking region. Non-uniform field may degrade the tracking quality somewhat but not seriously enough. Besides, the field quality could be improved by introducing graded winding of coil as has been done in ZEUS[11].

3.3 Need for muon toroids

In the 87 Berkeley LSD design, the momentum of a muon in the central region is measured with the use of magnetic field in the return yoke. In the present configuration, an additional iron toroid system outside the barrel calorimeter is introduced. In the P_t range below several hundred GeV/c, a precision measurement of muon momentum is done using inner tracking system, while the iron toroid system is useful for muon identification, high P_t triggering and redundant momentum measurement. In the central rapidity region, the

momentum of a muon is measured twice, inside and outside. This will minimize the contamination from mis-connections, π/K decays and punch-thorough hadrons. The muon toroid takes over for better momentum measurement above 1 TeV/c. The forward angle regions are covered by a forward muon toroid system with enough iron thickness for higher muon momenta.

3.4 Choice of calorimeter technology

There seem to be three major points to be considered.

Point 1: For any of large detector systems, a rather conservative approach must be taken in the choice of technology, since the system engineering will be one of important aspects and basic detector elements must therefore be well understood[12].

Point 2: The number of technologies utilized in the detector should be minimized in order to simplify both the operation and the data analysis. In fact, it becomes rather clear from suffering experiences in CDF that a single calorimetry technology should be used for EM and hadronic parts as well as for central and endcap regions.

Point 3: In the forward region, the radiation level is quite high exceeding 1Mrads per year[4]. Since survival of the detector is of prime importance for long stable operation of the experiment, the highest priority must be given to radiation resistivity of the calorimeter.

Point 1 suggests us that either LAr or scintillation calorimeter would be the choice at the present time. Point 2 tells us not to combine these two technologies. Point 3 tells us that LAr is the present choice of technology. In addition, we can list up advantages of LAr : no need of tower-by-tower calibration, stable operation, compatibility with magnetic field, large dynamic range and good linearity, fine granularity and longitudinal segmentation, homogeneous response, etc. It has been repeatedly pointed out that LAr may

exhibit its problems for its speed, the cryostat effect, and the e/h ratio. We will come back to these points later.

3.5 Hybrid tracking system

We propose a hybrid tracking system associated with a concept of separated tracking functions. In the present technology, there seems no single technology that can cover the entire tracking volume with three fold capabilities required for tracking, i.e. position resolution, pattern recognition and triggering. Wires (straws) can not be reliable enough in the region of small radii. On the other hand, a silicon strip system is good for small radii. Since position resolution by silicon strips is far better, it is good to rely on silicon system for momentum determination. On the other hand, silicon strips are not good for triggering and pattern recognition. Wire system is best suited for these two functions.

4. Structural considerations

There are three different stages to be considered for accessibility to the central part of the detector :

a. construction,

b. quick access for minor repairs,

c. major repair and later upgrade.

It is obvious that quick access for minor repairs should be done without moving the entire detector from the beam line. It is also better to do major repair and/or upgrade without interfering accelerator operation. Since the revised SSC design contains bypass lines for such occasions, there is no more need for moving the entire detector out of beam line. Therefore the remaining problems to be solved is how to gain access to the various part of the detector. As illustrated in Fig.3, we have considered three extremes ;

CASE 1 : Split entire detector into three parts, one barrel and two endcaps (MAC, CELLO).

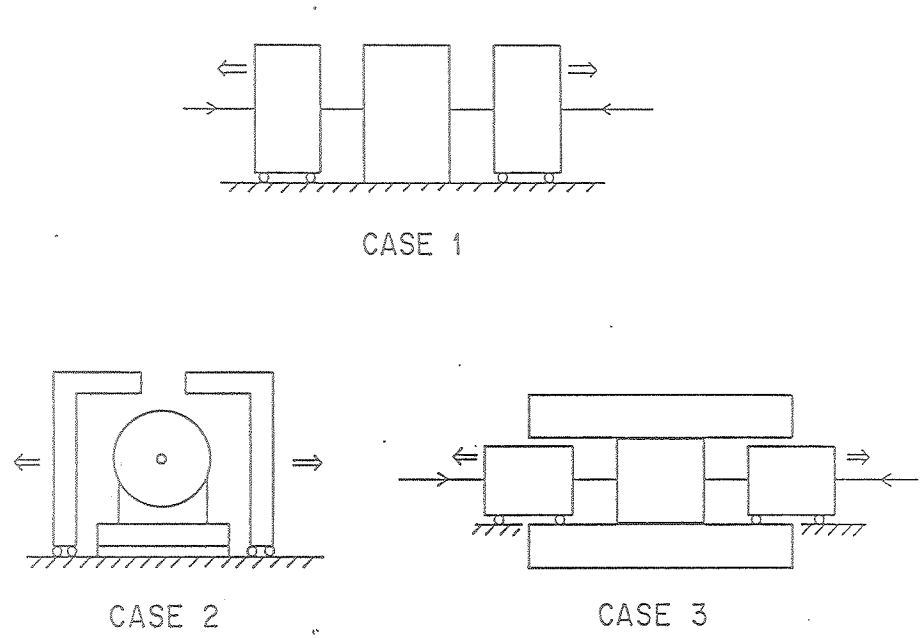

Fig.3 Three ways of access to the central part of the detector.

Table 1. Weight of detector components.

detector part	number	H x W x L	weight	
inner tracker	1	3.2 x 3.2 x 8 m^3	< 5 t	movable
barrel calorimeter	1	9 x 9 x 8 m^3	3400 t	movable
endcap calorimeter	2	8 x 8 x 3 m^3	1300 t	movable
air core solenoid	1	4 x 4 x 8 m^3	20 t	movable
barrel muon toroid	1	16 x 16 x 24 m^3	19000 t	fixed
endcap muon toroid	2	9 x 9 x 4 m^3	2000 t	movable
forward detector	2	m^3	1000 t	movable
total			31020 t	

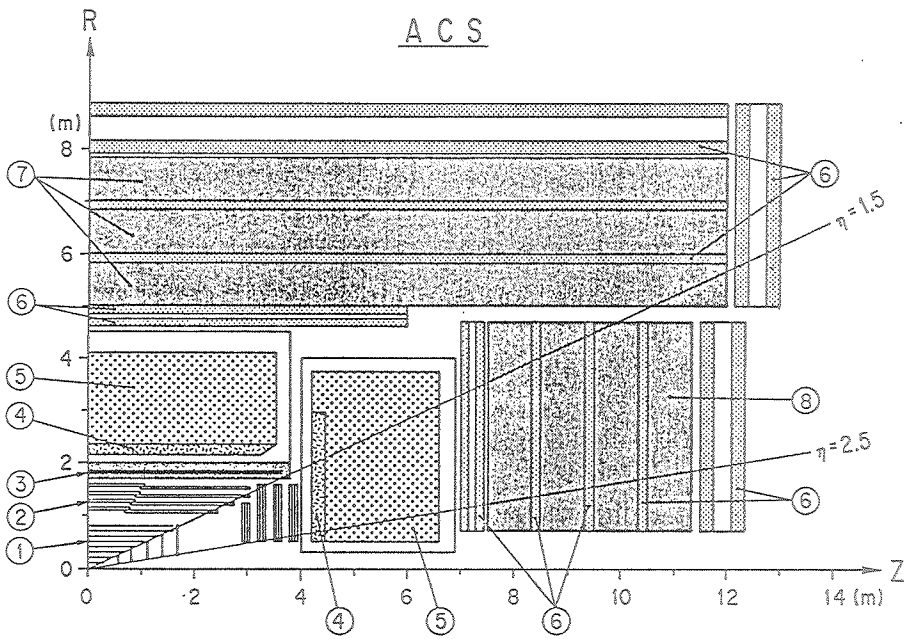

1. Silicon microstrip tracker
2. Straw wire tracker
3. Superconducting air-core solenoid
4. EM liquid argon calorimeter
5. Hadron liquid argon calorimeter
6. Muon tracker
7. Barrel iron toroid
8. Endcap iron toroid

Fig.4 Layout of the ACS detector along the beam.

CASE 2 : Split muon detectors into left and right along the beam line (JADE, UA1, ZEUS, H1).

CASE 3 : Gain access by opening the endcap (L3, DELPHI, ALEPH, VENUS, TOPAZ, AMY).

Our major concern is that the scales of the detector (~30 ktons, 15-20m high) are substantially larger than any of existing detectors. Moving heavy and tall objects thus becomes one of major issues. It would be better if we could minimize the weight and physical size of each movable part for easy access. The muon toroid weighs far most in the system. As a consequence, it is not wise to employ cases 1 or 2, in which the muon toroid must be movable. We propose to fix the heaviest muon part in the experimental hall (like L3), and make only the front and back endcap part movable. A natural consequence of this selection is that the barrel muon toroid extends to the both end of the detector as shown in Fig.4. Table 1 lists up the approximate size and weight as well as movability of detector parts. It should be noted that, with the present selection of geometry, the maximum size/weight of the movable components are now reduced to 9m/3400tons from 16m/8000tons for the cases 1 and 2. They are considered to be manageable with small extrapolation from existing detectors. Fig.5 shows an example of the rail system for a movable part. A sliding mechanism is provided by a plastic plate called "oilless fiber freon". It has a good mechanical strength as well as a low friction coefficient[65]. Use of tirtanks is less attractive because of limitted space availability for the present mass scale. Assembly is another main aspect to be seriously considered from the beginning of the design. In the proposed scheme, assembly of barrel muon toroids and installation of muon chambers are done in parallel with assembly of calorimeters and forward muon toroids. As illustrated in Fig.6 for an example of experimental and assembly halls, these major components which weigh more than 500tons should be assembled underground close to the final

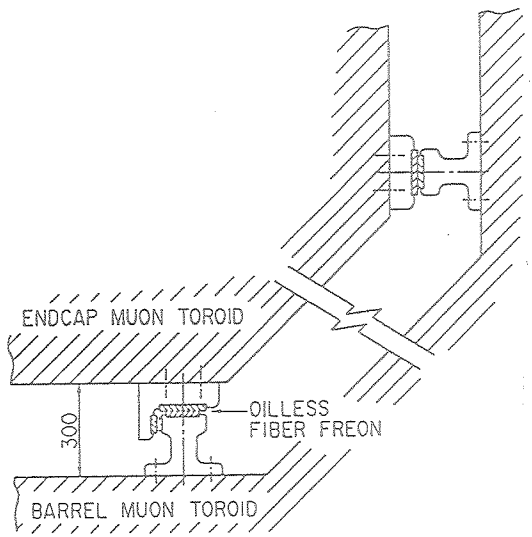

Fig.5 Sliding mechanism using oilless fiber freon.

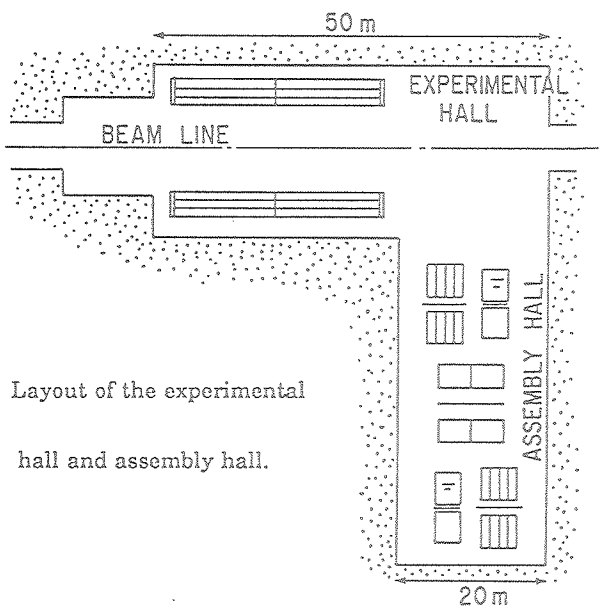

Fig.6 Layout of the experimental hall and assembly hall.

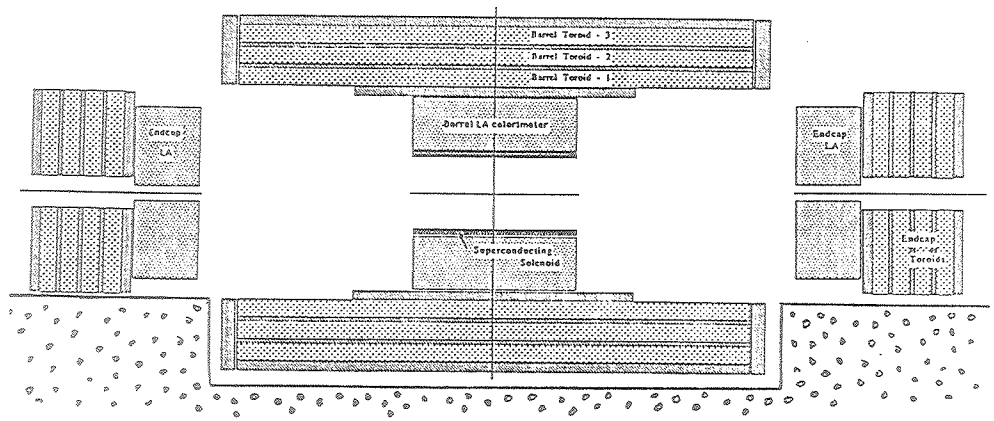

Fig.7 Access to the central part of the detector.

Table 2. Summary of existing solenoids for Colliding beam experiments, where B = central field, L = radiation thickness, E = stored energy, M = cold mass and R = E/M.

experiment	B(Tesla)	L(X_0)	E(MJ)	M(ton)	R(kJ/kg)
CDF	1.5	0.84	30	5.6	5.4
TOPAZ	1.2	0.70	20	4.0	5.0
VENUS	0.75	0.52	12	4.3	2.8
CLEO-II	1.5	?	25	7.0	3.6
ALEPH	1.5	2	137	25	5.5
DELPHI	1.2	7.4	108	25	4.3
H1	1.5	1.6	188	?	?
ZEUS	1.8	0.95	16	1.9	8.4

detector location. After assembly, these major components are transported using rails into the detector as sketched in Fig.7.

5. Superconducting Solenoid

5.1 Coil thickness

Based on the construction experiences of the thin superconducting solenoids for CDF[13], TOPAZ[14] and VENUS[15] and more recently for Astromagnet[16] and ZEUS[11], we estimate how thin a superconducting coil can be made using existing technology. Table 2 lists the existing solenoids in terms of central field and radiation thickness, indicating that a 2T solenoid with radiation thickness of less that $1X_0$ is within the reach of present technology.

We introduce a new design concept for thin solenoids that helps in minimizing the coil thickness. If one is able to maximize the ratio

$$R = \frac{E(\text{stored energy})}{M(\text{active cold mass})}$$

then the coil thickness could be minimized. When a quench occurs associated with a failure of the energy extraction to an external energy dump, i.e. if the worst case happens, all the stored energy must be dumped in the cold-mass of the magnet. As a consequence, the temperature of the coil rises. If the temperature rise in the coil exceeds 100K, the solenoid might suffer severe thermal stress. This should be avoided for safety reason. Now suppose a uniform energy dump is realized over the entire cold mass of the magnet in a short enough time, we get

$$R = \frac{E}{M} = H(T_1) - H(T_0)$$

where H is the coil enthalpy, $H = \int C_p dT$. By setting T_1=80K and T_0=4K, we obtain

$$R = H(80K) - H(4K) \cong 10 \text{ kJ/kg}$$

The ratios R for existing magnets are also shown in Table 2, in which one notices that the R values of most of detector solenoids are at around 5 kJ/kg. This indicates a room for improvement, i.e. an increase of R to 7 to 10 kJ/kg, if one can introduce a mechanism of avoiding localized energy dump at a time of quench in conjunction with a failure of the energy extraction. We propose an introduction of thin pure-aluminum axial strips as stated below.

5.2 Design of superconducting solenoid [17]

The present design is for the coil radius of 1.8m with the central magnetic field of 2T. Two-phase indirect Helium cooling is chosen based on the experiences of thin solenoids for CDF, VENUS and TOPAZ. However the thermo-siphon technique is another viable option[18]. We aim the operating current of 10,000 amperes to keep the total inductance low. The residual resistivity ratio (RRR) of the aluminum stabilizer of the coil is kept below 1000 to maintain the structural strength. According to the concept introduced above, we raise the ratio R of stored energy to cold mass by a factor of 1.5~2 to minimize the thickness of the magnet. Table 3 summarizes the main parameters of the present design.

In our recent R&D work, we have noticed an enhancement of the axial quench propagation due to the use of thin axial liners of pure aluminum[19]. This enhancement of the quench velocity in the axial direction enables the stored energy to be more uniformly dumped in the coil and therefore suppresses the maximum temperature rise in the coil.

A recent R&D work also made it possible to use a honeycomb structure of aluminum alloy for the outer vacuum wall of cryostat[16]. This will help in reducing the effective thickness of the magnet.

Fig.8 illustrates the cross section of the solenoid including the proposed end structure. It is necessary to occupy a radial space of 29 cm in order to take

Table 3. Coil parameters

Inner radius of cryostat	1700 mm
Outer radius of cryostat	1990 mm
Total length of cryostat	8000 mm
Radius of coil at 4.5 K	1800 mm
Length of coil at 4.5 K	7560 mm
Weight of the coil and cryostat	20 t
Weight of the cold mass	16 t
Central Field B(Z=0)	2 Tesla
NI	13.4 MAt
Nominal operating current	10,000 A
Stored energy	120 MJ
Stored Energy/effective cold mass	7.5 kJ/kg
Self inductance	2.4 H
Superconductor	NbTi/Cu (0.55/0.45)
Stabilizer	Al (RRR=750)
Coil cross section	5.6×40 mm^2
NbTi/Cu matrix	2×4 mm^2
current density in NbTi	2300 A/mm^2
Current density in NbTi/Cu matrix	1250 A/mm^2
Overall current density	45 A/mm^2
Load line ratio (I_{op}/I_c) at 5 K	80%
Insulation material	Kapton/Glass lamination
Turn to turn thickness	0.2 mm
Thickness of axial aluminum strips	2 mm
Thickness of support cylinder	28 mm
Total radiation thickness	1.12 X_0
Total interaction length	0.25 λ_0
Thermal load at 4.5 K	55 W + 33 l/hr

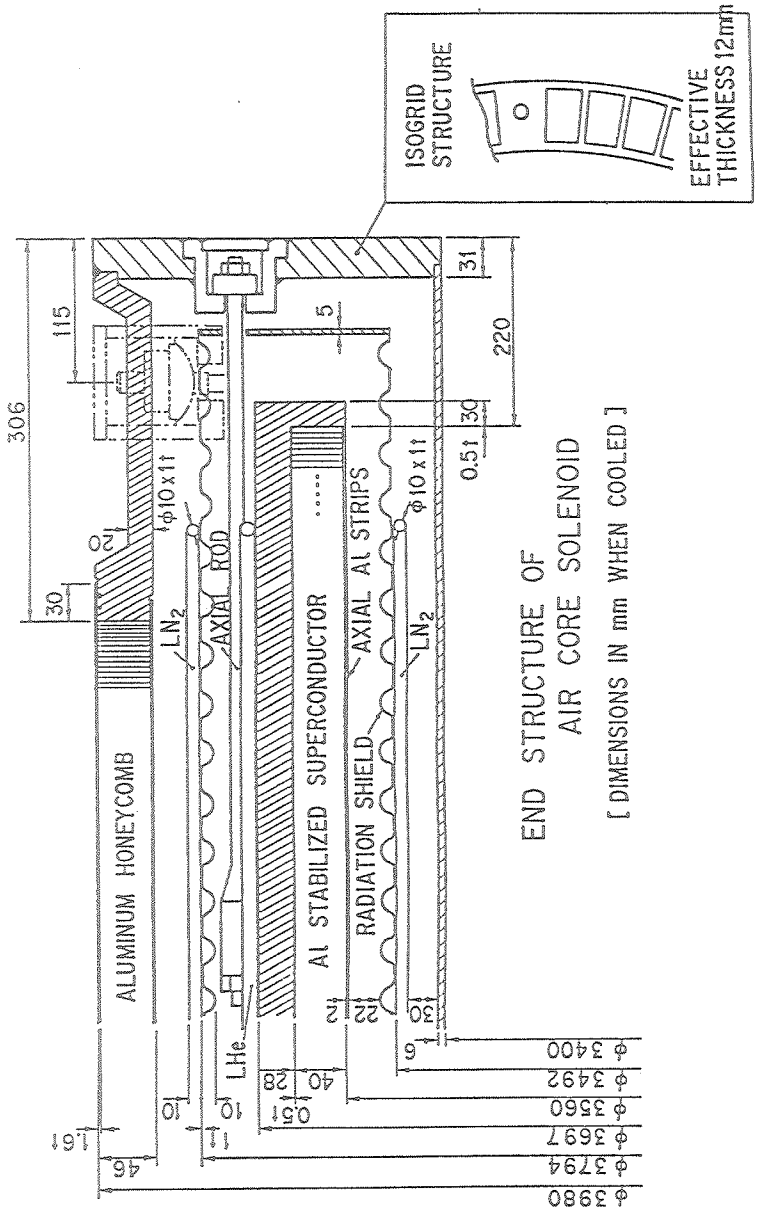

Fig.8 Cross section of the thin solenoid showing the end structure.

into account the coil shrink when it is cooled. Table 4 gives details of the coil thickness in terms of radiation and interaction length[20]. The design employs a conventional supporting technique using axial rods in one end and radial rods in both end. There must be a transition from the Al-honeycomb to a cylinder near the cryostat ends. As shown in Fig.8, the aluminum end cylinder and/or endcap plates will be scraped off (isogrid structure) to minimize the material thickness while keeping the structural strength adequate. We have obtained the average density of $\rho_{AV} \cong 0.35\ \rho_{AL}$ for the endpart of the magnet by summing up the weight of the components. This number is very close to the average density of $0.33\ \rho_{AL}$ in the central part of the solenoid.

5.3 Magnetic field profile

Fig.9 show the results of the POISSON for magnetic field. Return yokes are muon toroids in the present case as shown in the figure. The field profile obtained is not so different from that of air-core solenoid since the return yokes are far away. Fig.10 depicts the contour of equal strength of the magnetic field. The effect of non-uniform magnetic field will be discussed in the tracking section.

It is worth pointing that the field strength in the calorimeter region is rather low. In most of the barrel calorimeter region, we observe B=0.02 to 0.3T, while in the endcap calorimeter area, we get 0.25 to 0.85T. If pulse transformers for liquid ionization calorimeters can be shielded properly up to the filed of 0.5T, there is a hope that one can use ferrite transformers for most part of the calorimeters[21].

5.4 Forces on the coil

Using the program Poisson, we have obtained forces on the coil for the case of B=2T as summarized in Table 5. These values are very close to those of hand calculations for an air-core solenoid. It is noted that the force on return yokes

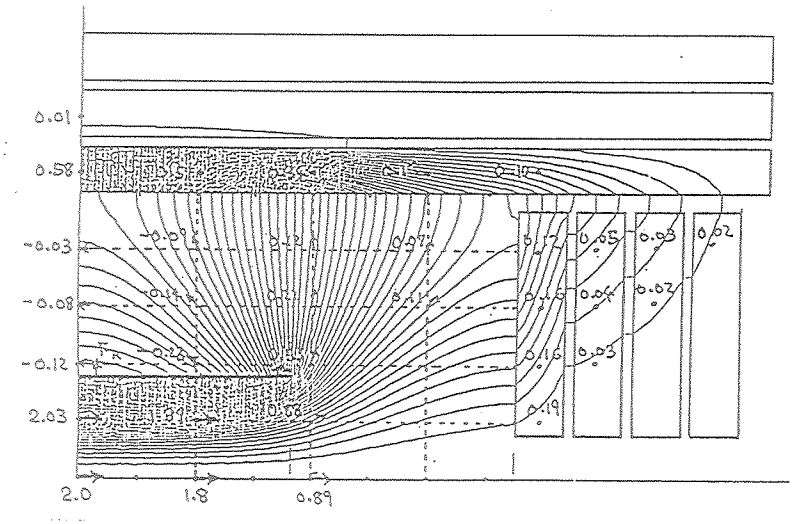

Fig.9 Magnetic field lines of the air-core solenoid.

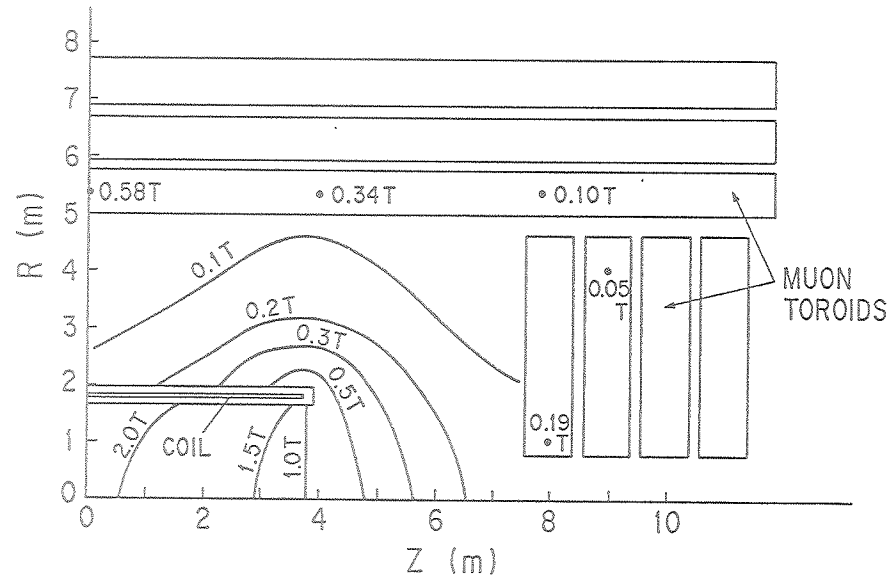

Fig.10 Lines of constant strength of the magnetic field.

Table 4. Thickness of the solenoid

element (material)	equiv-thickness	X_0	λ_0
Al-Honeycomb (Al alloy)	6 mm	0.074	0.0236
Outer Radiation Shield (Al)	1.6 mm	0.018	0.0041
Support Cylinder (Al-alloy)	28 mm	0.345	0.0737
Aluminum Stabilizer (Al)	39 mm	0.438	0.0990
Superconductor (Cu)	1.4 mm	0.098	0.0093
Insulation (GFRP)	2 mm	0.011	0.0038
Axial Al Strips (AL)	2 mm	0.022	0.0051
Inner Radiation Shield (Al)	1.6 mm	0.018	0.0041
Inner Vessel (Al)	6 mm	0.074	0.0236
Miscellaneous	---	0.020	0.0072
Total	290 mm	1.12	0.254

Table 5. Magnetic Forces on the coil.

F_{AX}	Axial compressive force	1850 tonf at the coil center
P_{HP}	Magnetic hoop force	16 kg/cm^2
F_{YK}	Axial force on return yoke	60 tonf
dF_z/dz	Axial de-centering force	1.6 tonf/cm of deviation
dFr/dz	Radial de-centering force	? (small)

Table 6. Stress, strain and the allowable stresses of aluminum alloys.

Hoop Forces		σ_f (coil)		4 kgf/mm^2	
		σ_f (cylinder)		7.3 kgf/mm^2	
		strain		0.086 %	
Axial Force at z = 0		σ_z (coil)		−2.8 kgf/mm^2	
		σ_z (cylinder)		−3.4 kgf/mm^2	
		strain		−0.041 %	
material	pure Al (RRR=750)	2219T851	5083-O	6063T5	
Youngs Modulus	6900	8500	~7500	7700	kgf/mm^2
Yield Strength	4	48.4	17.8	> 20	kgf/mm^2
Allowable stress	~ 2.7	~ 32	~ 12	~ 13.3	kgf/mm^2

F_{YK} and the axial de-centering force dF_z/dz are quite small, in contrast with the case of a solenoid with iron flux returns close to the end of magnet. The radial magnetic pressure P_{HP} as well as axial compression force F_{AX} must be supported by a combination of the support cylinder and superconducting coil. The radial de-centering force is not calculated but it is expected to be small.

We used a simplified stress-strain curve in calculating the approximate stress and strain[22]. The results are summarized in Table 6. One sees that the hoop force generates the most stringent stress. The stress on support cylinder thus obtained is below the allowable stress as shown in the same table. However, the pure aluminum part of the coil will undergo inelastic strain cycles. Its effect on RRR is being studied.

It is noted that part of the axial force on the conductor must be transmitted to the support cylinder through the ground insulation layer between the coil and the cylinder. The shear stress in the insulation layer is maximum near the coil edge. A rough estimate of this shear stress is 0.4kgf/mm^2. The shear strength of ground insulation material with adhesive (epoxy) has been studied in the past. The results of a full size model coil for the TOPAZ magnet, indicated more than 2.5 kgf/mm^2 in shear strength at low temperature, indicating that we have enough safety margin[23].

5.5 Quench simulation

We have performed a quench simulation in order to evaluate the safety margin of the proposed solenoid, using a program QUENCH. A quench is assumed to start at the edge of the coil for the worst case. Fig.11 illustrates the time sequence of the current, voltage and temperature of the coil for two extreme cases, one with a successful energy extraction and other with a failure of the extraction. Fig.12 shows the dependence of the maximum and minimum temperature at the worst case quench without energy extraction as a function of the thermal conductivity ratio in z to ϕ directions. This ratio will be enhanced

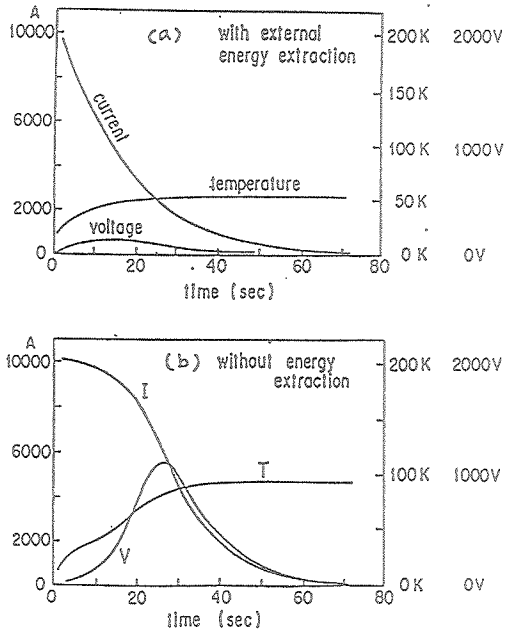

Fig.11 Results of quench simulation for the case (a) with external energy extraction and (b) without it.

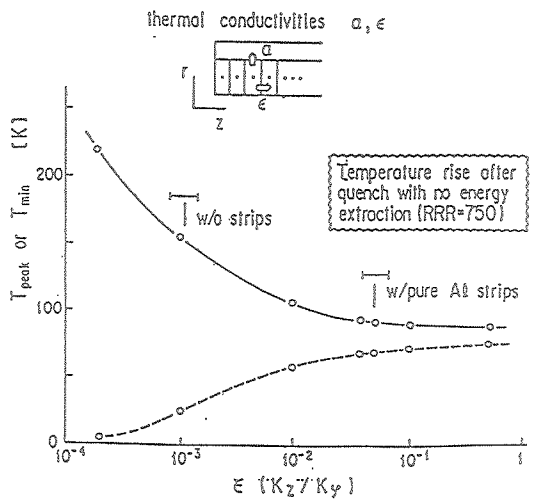

Fig.12 Dependence of the maximum and minimum temperature rises as a function of the thermal conductivity ratio in z to φ directions. This is for the worst case corresponding to a failure of the energy extraction.

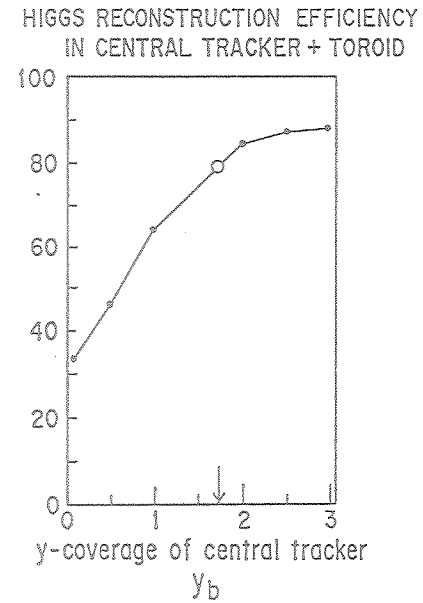

Fig.13 Relative detection efficiency of $H \to ZZ \to \mu\mu\mu\mu$ as a function of rapidity range covered by the central tracker associated with muon toroid

Table 7. Relative detection efficiency of $H(500GeV/c^2) \to ZZ \to \mu^+\mu^-\mu^+\mu^-$
main cuts : $P_t > 20GeV/c$, $|y_\mu| < 3$, $|M_Z^{\mu\mu} - M_Z| < 6\ GeV/c^2$

case		$\Delta P_\mu/P_\mu$	efficiency
1	perfect resolution	0.00	1.00
2	ideal L3 type	0.02	1.00
3	electron resolution	$0.15/\sqrt{E}$	1.00
4	high resolution tracker	0.3Pt	0.99
5	ideal EMPACT type	0.04	0.97
6	hybrid tracker	0.14P + 0.01	0.88
7	straw tube tracker	0.54Pt	0.82
8	L* type	0.02 (|y|<1) and 0.02+(|y|−1)*0.06 (|y|>1)	0.80
9	thick iron toroid	0.1+0.1PT	0.35
10	thin iron muon toroid	0.2	0.11

by a factor of 50 if we introduce the aluminum axial strips. It is clear from this plot that the axial strips help in equalizing the temperature rise and thus reducing the maximum temperature below 100K during the worst case quench.

6. Muon Detector

6.1 Detection of H→4μ

In order to evaluate necessary momentum resolution for muons, we calculated detection efficiency of H→ ZZ →μμμμ as a function of muon momentum resolution for m_H=500 GeV/c^2 [24]. Table 7 is the list of the relative yield of Higgs detection for various set of momentum resolution. The main cuts are listed in the same table. One notices that the efficiency drops sharply down to 0.35 (case 9) if the iron toroids are used for momentum measurement because the μμ invariant mass resolution becomes wider than the Z mass cut (±6GeV) employed. This has been pointed many times why an air-core toroid or a large muon solenoid is better compared with iron toroid system. However it is interesting to note that the invariant mass resolution of two isolated muons can be improved by the inner tracking system for the central rapidity region. Fig.13 shows detection efficiency as a function of rapidity range covered by the central tracker. This indicates that , as far as Z→μμ detection for H→4μ is concerned, the proposed solenoid system with iron muon toroids is comparable to other specialized designs.

6.2 Muon hit rate and triggering

We calculated the rate at muon detector including punchthroughs and π/K decays in addition to prompt muons[25]. Hadron punchthrough probability in the calorimeter (assumed 2m solid iron for this calculation only) is based on the WA1 fit for thin iron and the Lang fit for thick iron[26]. Two different muon rates are given, one at the calorimeter exit and other at the exit of the muon

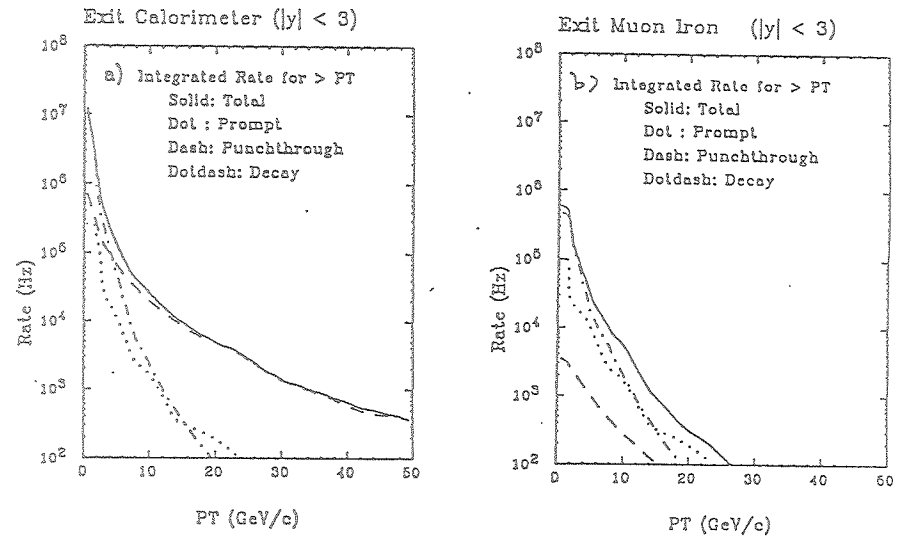

Fig.14 Integrated hit rate at the exit of calorimeter (a) and at the exit of muon filter(b). The rates are summed up to |y|=3. p_t for prompt and decay muons are those of muons while p_t of parent hadrons are used for punchthrough.

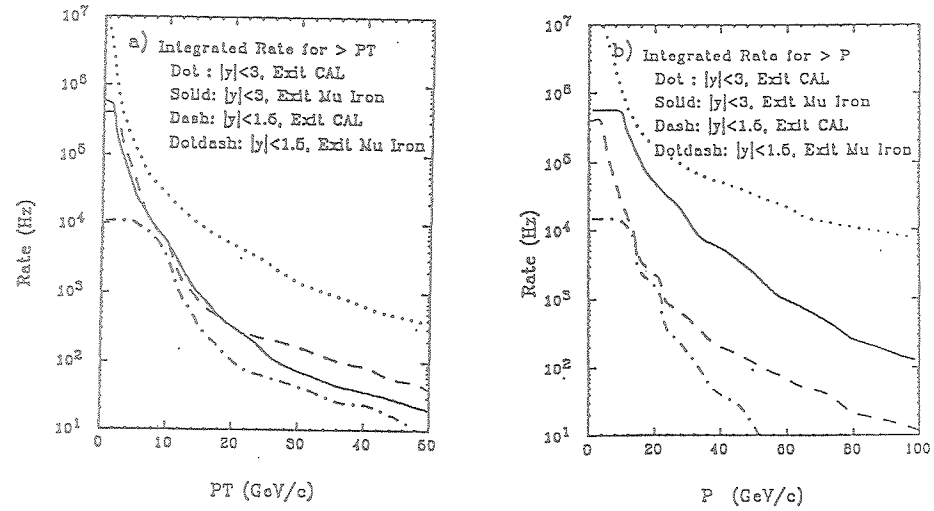

Fig.15 Integrated muon rate vs threshold in (a) p_t or (b) p of muons for: at exit of calorimeter and muon filter; and |y|<3 and 1.5.

filter (2.5m thick iron is assumed in the barrel region and 3.5m thick iron in endcap). Table 8 summarizes the overall hit-rate integrated over $|y|$ to 1.5 or 3.0, while Figs.14a and 14b show integrated rates at the exit of calorimeter and muon filter. It is obvious from these table and figures that low energy muons mainly from π/K decays dominate the rate. Figs.15 summarize integrated rates for four cases. Muon trigger is one of essential triggers and the 1st level muon trigger rate must be suppressed to the level below 1 kHz to be realistic. Thus these results indicate a necessity of thick absorber in addition to calorimeter (~10 λ_0) and a necessity of rejection of muons with $p_t < 20$ (or $p < 40$) GeV/c in the level 1 trigger. These requirements can be well realized simultaneously by introducing thick muon toroid system in conjunction with triggering devices.

6.3 Design of muon toroid system[27]

As shown in Fig.16, the octagonally shaped structure of barrel muon toroids is mechanically more stable and easier in its construction. The total thickness is chosen to achieve close to 10% momentum resolution in the momentum range up to several hundred GeV/c[28]. Two middle gaps are introduced for better muon identification, better linkage of track segments and better momentum resolution as shown later. Frequent sampling along a muon trajectory is needed for a TeV muon because of rather high probability of associated showers [29]. Fig.17 illustrates how each layer of the barrel octagonal toroid can be constructed from the floor with thick iron plates. Each layer of iron is made of 3 layers of iron block of approximately 5m×3.5m×0.28m (~38 tons). Three layers of octagonal structures are held in place by spacers placed every 3m or so along the axis and at each apex of the octagon as illustrated in Fig.18. Spacers are arranged such that there are no completely dead regions when looked from the interaction point. The endcap toroid consists of 4 layers of octagonal iron plates as is sketched in Fig.19. Muon chambers are placed in front, in between and at the back of these plates.

Table 8. Overall muon rates

y range	Exit at	Prompt(Hz)	Decay(Hz)	Punch(Hz)	Total(Hz)
$\|y\| < 3$	CAL	1.3×10^5	1.1×10^7	5.3×10^5	1.2×10^7
$\|y\| < 3$	μ filter	1.1×10^5	5.3×10^5	3×10^3	6.4×10^5
$\|y\| < 1.5$	CAL	1.5×10^4	2.8×10^5	4×10^3	3×10^5
$\|y\| < 1.5$	μ filter	2.6×10^3	9×10^3	5×10^1	1.2×10^4

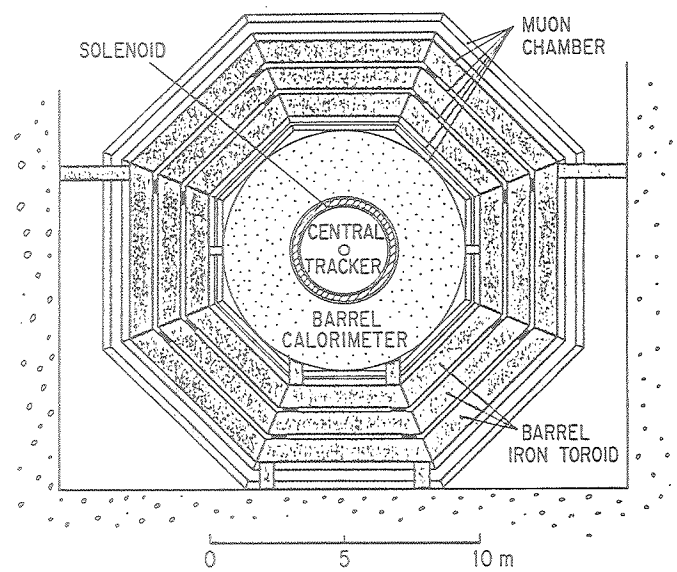

Fig.16 Layout cross section normal to the beam.

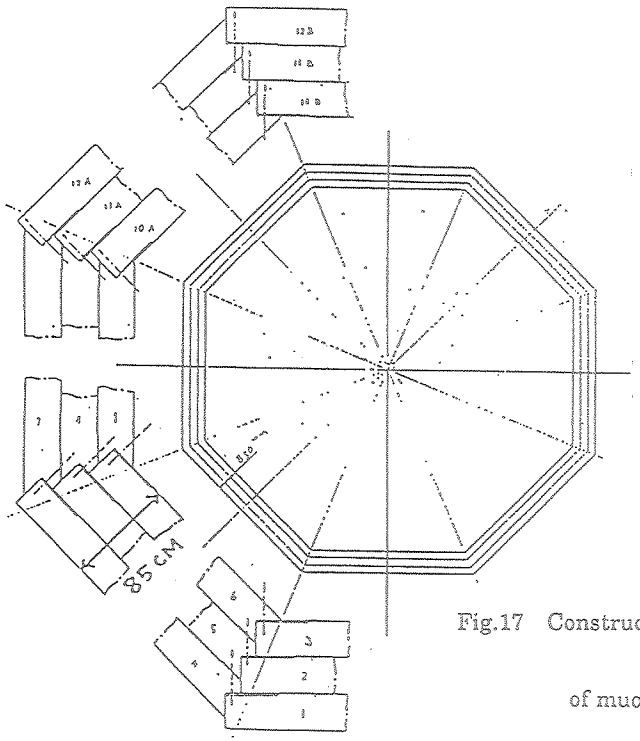

Fig.17 Construction of each layer of muon barrel toroid.

Table 9. Parameters of toroidal coil

coil location	endcap	1st barrel	2nd barrel	3rd barrel	
turns/octant × current	6×5000	6×4666	8×5250	12×4666	Aturn
[2T]	[6×13333	6×12333	8×13000	12×10000	Aturn]
magnetic field	1.77~1.84	1.67~1.80	1.70~1.82	1.75~1.82	Tesla
[2T]	[1.95~2.20	1.83~1.97	1.87~1.98	1.87~1.95	Tesla]
total coil length	900	2400	3200	4800	m
total resistance	0.0035	0.0093	0.0124	0.0186	Ω
voltage difference	17.5	46.5	62.0	93.0	V
flow of cooling water	1.05	2.79	3.71	5.56	*l*/sec
pressure drop	0.22	0.48	0.16	0.4	MPa
power dissipation	88	233	310	465	kW
temperature rise	20	20	20	20	°C

note : coil material copper ($\rho = 1.55 \times 10^{-8}\ \Omega\cdot m$, $i = 125 A/cm^2$)
inlet temperature of cooling water 30°C
outlet temperature of cooling water 50°C
[ ] indicates for the case of 2 Tesla.

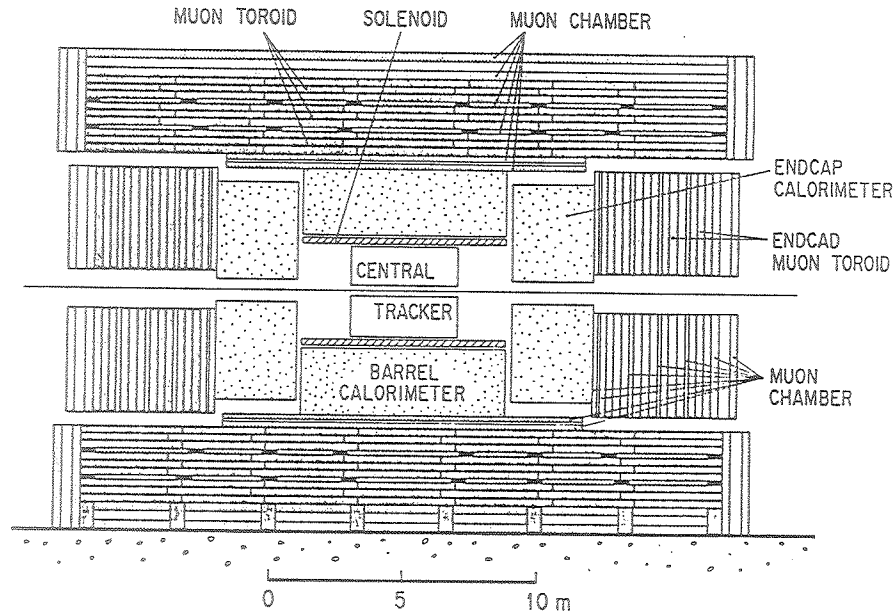

Fig.18 Cross section of muon toroid system showing unit pieces of iron blocks and spacers.

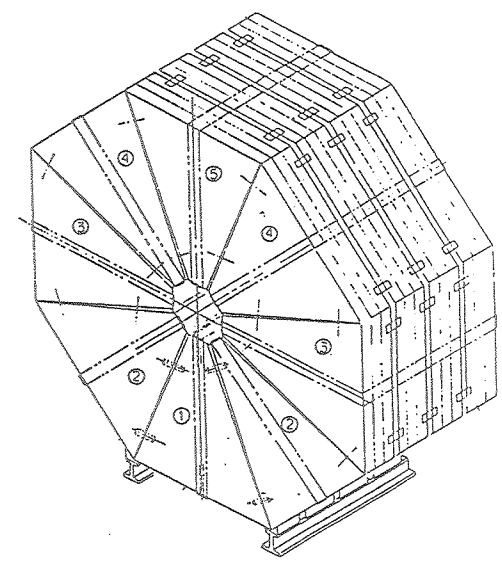

Fig.19 Sketch of the endcap toroid.

Magnetic field in the iron plates is calculated using programs JMAG2D and JMAG3D. It might be better to keep the toroidal field as uniform as possible for efficient on-line triggers and for smaller corrections. In order to obtain uniform magnetic field, the current and coil location are adjusted as shown in Fig.20 for the barrel toroids. For the endcap toroids, the field uniformity can be improved by introducing a wedge shaped nonmagnetic material such as SUS304 as shown in Fig.21. Copper hollow conductors are used for coils. Table 9 summarizes the parameters of muon toroids in the case of field strength of ~1.8T [2T].

6.4 Muon momentum resolution [30]

Fig.22 shows the momentum resolution σ_K/K, where $K=1/p_\mu$, at 90° obtained by a Monte Carlo and a track fit program. Effects of multiple scattering in the toroids and in the calorimeter are included. Six chamber planes in front, three in each gap, and 6 at the back of the toroid are supposed to exist. A modest chamber resolution of 300μm is assumed by taking the large spans to be covered by these chambers into account. At low energies, the resolution is limited to ~12% by multiple scattering. Three different cases shown in the figure indicate a big resolution improvement by muon chambers in the middle gap as well as by vertex connection at high energies. Rapidity dependence is shown in Fig. 23 for 1 and 2 TeV/c muons. The resolution in the forward region is much better than that at 90° due to effectively thicker toroids. Above a few hundred GeV, the radiative processes (brems, pair production and photo-nuclear interactions) dominates the muon energy loss. GEANT was used to evaluate the effect as shown in Fig.24. The fitted momentum distributions are skewed and shifted due to the radiative processes. More studies are clearly needed.

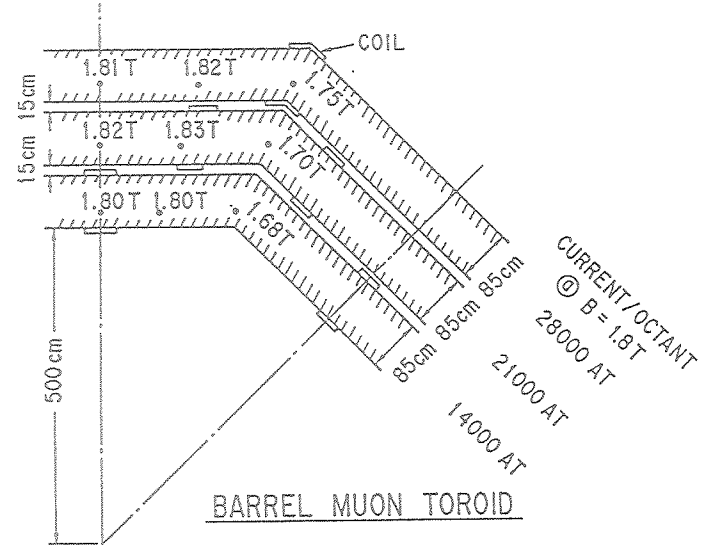

Fig.20 Cross section of barrel muon toroid. The location of coil is adjusted to achieve better field uniformity.

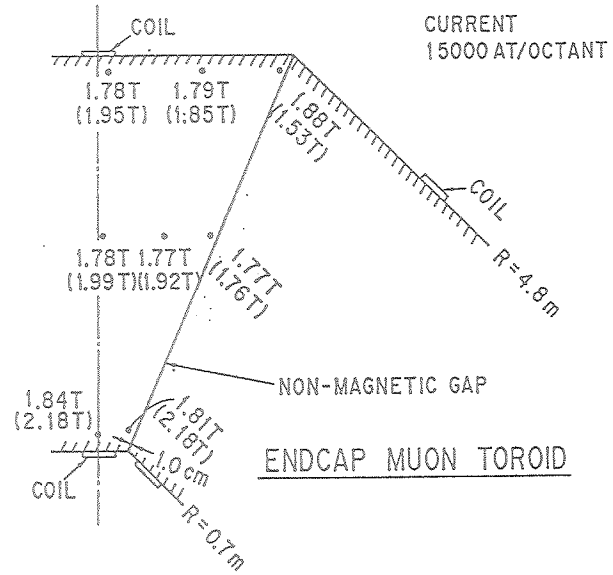

Fig.21 Design of endcap toroid. A tapered non-magnetic insert is placed at each edge to increase field uniformity.

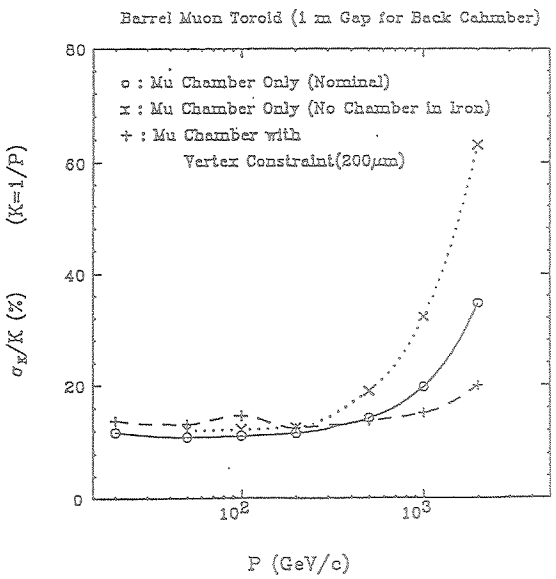

Fig.22 Momentum resolution σ_K/K where $K=1/P$ as a function of momentum at 90° for position resolution of 300μm for muon chamber. Three different set of data are assumed as shown.

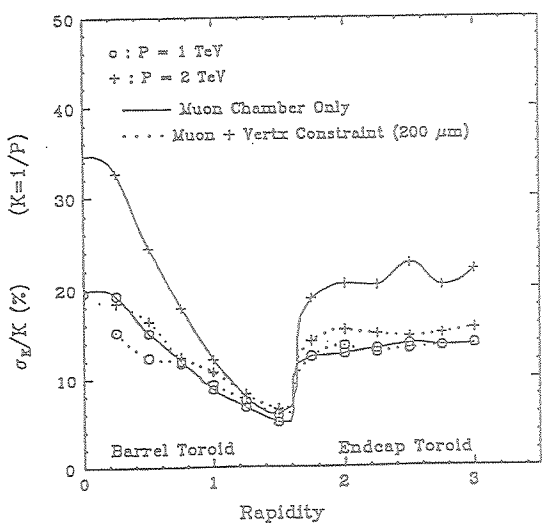

Fig.23 Rapidity dependence of the muon momentum resolution at 1 and 2 TeV/c.

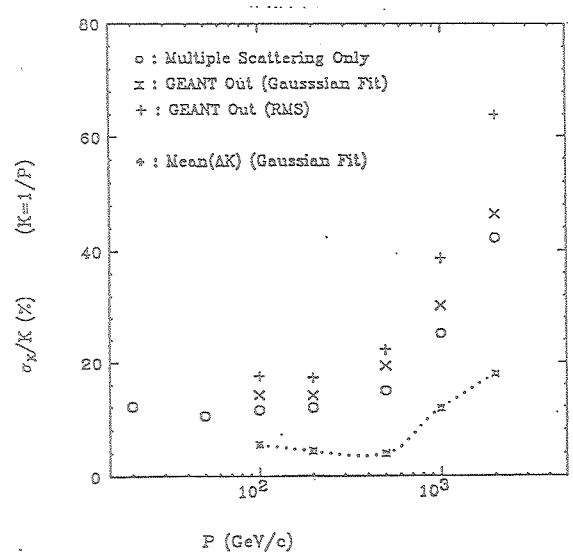

Fig.24 Muon momentum resolution through GEANT simulation.

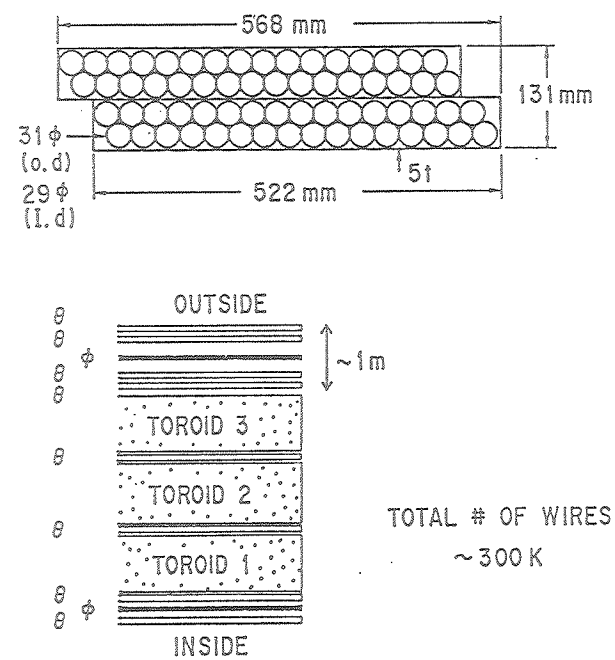

Fig.25 Cross section of muon chambers and their layout.

Table 10a Barrel Muon System

layer #	chamber	r	wire length	Ntube × layer × Ldiv × oct
1- 4	θ	457.5 cm	380 cm	800 × 4 × 1 × 8 = 25600 tubes
5- 8	ϕ	475.0	800	125 × 4 × 3 × 8 = 12000
9-12	θ	492.5	405	800 × 4 × 1 × 8 = 25600
toroid #1		500~585		
13-16	θ	592.5	490	800 × 4 × 1 × 8 = 25600
toroid #2		600~685		
17-20	θ	692.5	570	800 × 4 × 1 × 8 = 25600
toroid #3		700~785		
21-24	θ	792.5	655	800 × 4 × 1 × 8 = 25600
25-28	ϕ	835.0	800	220 × 4 × 3 × 8 = 21120
29-32	θ	877.5	725	800 × 4 × 1 × 8 = 25600
				total 186720 tubes

Table 10b Endcap Muon System

layer #	chamber	z	wire length	Ntube × Nlayer × Nblock
1- 6	r	708.0 cm	60~400 cm	200 × 6 × 8 = 9600 tubes
7-10	x	720.0 cm	200~480 cm	240 × 4 × 4 = 3840 tubes
11-14	y	728.0 cm	200~480 cm	240 × 4 × 4 = 3840 tubes
15-20	r	736.0 cm	60~400 cm	200 × 6 × 8 = 9600 tubes
toroid #1		750~835 cm		
21-26	r	842.5 cm	60~400 cm	200 × 6 × 8 = 9600 tubes
toroid #2		850~935 cm		
27-32	r	942.5 cm	60~400 cm	200 × 6 × 8 = 9600 tubes
toroid #3		950~1035 cm		
33-38	r	1042.5 cm	60~400 cm	200 × 6 × 8 = 9600 tubes
toroid #4		1050~1135 cm		
39-44	r	1150.0 cm	60~400 cm	200 × 6 × 8 = 9600 tubes
45-48	x	1196.0 cm	200~480 cm	240 × 4 × 4 = 3840 tubes
49-52	y	1204.0 cm	200~480 cm	240 × 4 × 4 = 3840 tubes
53-58	r	1250.0 cm	60~400 cm	200 × 6 × 8 = 9600 tubes
			total number of tubes / endcap	82560 tubes

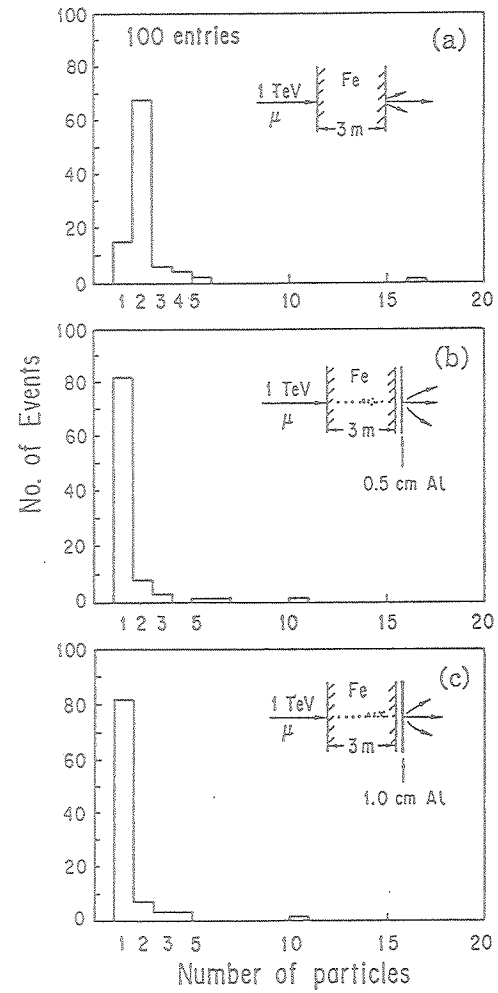

Fig.26 Number of particles seen at the exit of 3m iron plates for penetrating muons of 1 TeV/c with (a) no soft absorber, (b) 0.5 cm thick Aluminum plate and (c) 1.0 cm thick.

6.5 Muon chambers

Fig.25 illustrates the proposed chamber configuration. For simplicity, we propose here to use drift tubes but it is not necessarily the optimum choice. For the barrel part, 64 tubes with outer diameter of 31mm are packed in an extruded aluminum module for construction and relative alignment. By arranging θ and ϕ chambers as shown in the figure, total number of sense wires is 187K as summarized in Table 10a. Scintillation counters are needed for triggering purpose but not considered yet. For the endcap system, we supposed use of smaller tubes with diameter of 2cm to cope with higher flux. Chamber types are r,x and y named by their measuring coordinates. Table 10b shows the configuration. Total number of sense wires is 165K.

Muons of ~1TeV or above frequently generate local showers in calorimeters and iron absorbers and thus disturb the track measurement[29]. It looks not easy to introduce magnetic field to clean up these low energy components in the present configuration[31]. Effects of soft absorbers at the exit of iron absorbers are estimated for 1 TeV muons by using GEANT[32]. As shown in Fig.26, a half cm of aluminum plate is effective in reducing soft associated particles.

7. Liquid Argon Calorimeter

7.1 Why liquid argon?

It has been pointed out that liquid argon (LAr) might be too slow in the SSC experiments. However the question raised is not "what technology is the fastest?" but "what technology is the best for physics outputs?". There are many advantages in using the LAr technologies:

- survival
- uniform response
- easy transverse and longitudinal segmentation
- no need for tower-by-tower beam calibration
- compatibility with magnetic field

- established technology.

Some of them might be more essential than the signal speed. There are three points to be answered for employing LAr as a calorimeter, its speed, the cryostat effect, and the e/h ratio. The necessity of fast response is to minimize the background as well as event pileup. Radeka has pointed that there is a way for effectively obtaining fast readout of LAr with amplifiers attached to detectors and with fast shaping circuits[33]. This has been demonstrated by the Helios experiment. We will estimate the pileup effect later.

A conceptual study of large LAr cryostats has been done to show the mechanical feasibility[34]. We follow the conclusion of this study that, among three different configurations, nose, endcap and endplug, the endcap is the best for hermeticity. Lead will be used as calorimeter absorber material for easier construction as well as the cost effectiveness. We discuss later the effects of e/h $\neq 1.0$. The calorimeter granularity is assumed to be $\Delta\eta\times\Delta\phi = 0.05\times0.05$ (ϕ in radian) at 90° based on the study on the W mass resolution[35]. At the forward region, this granularity corresponds to the tower size that is too small in comparison to the hadronic shower size. In the present design, the tower size similar to that of the barrel part is assumed as illustrated in Fig.27. Table 11 shows the outline of the configuration of the proposed LAr calorimeter together with readout tower numbers. Table 12 lists up typical detector capacitances.

7.2 Experience with VENUS LAr detector[36]

VENUS has two endcap units of EM LAr calorimeter. Each has 480 towers of 10 x 10 x 32 cm^3. Each tower has 4 longitudinal segmentations. Total number of readout electronics is 3840. They obtained the energy resolution of

$$\sigma_E/E = 11/\sqrt{E} + 1.4 \quad \%$$

using real $e^+e^- \rightarrow e^+e^-$, $e^+e^-\gamma$ reactions. Fig.28 is the plot of 30GeV Bhabha events. Surprisingly, this small constant term of 1.4% was obtained without any (beam or electronics) calibrations except one overall normalization

Table 11-a. Parameters of Barrel LAr calorimeter

name	r at 90° (cm)	Nlayer×(Ar+Pb) in mm	# of channels
vacuum vessel wall	200~202		
argon vessel wall	207~211		Nϕ×Nη×L/R×Interleaved
preamp & cabling	211~213		
EM layer # 1	213~218	12×(2+3)	128 × 27 × 2 × 1= 6912 ch
EM layer # 2	218~223	12×(2+3)	256 × 54 × 2 × 1= 27648 ch
EM layer # 3	223~236	20×(2+3)	128 × 27 × 2 × 1= 6912 ch
Hadron layer #1	236~276	50×(2+6)	128 × 24 × 2 × 2 = 12288 ch
Hadron layer #2	276~316	50×(2+6)	128 × 22 × 2 × 2 = 11264 ch
support & cabling	316~330		
Hadron layer #3	330~370	50×(2+6)	128 × 19 × 2 × 2 = 9728 ch
Hadron layer #4	370~410	50×(2+6)	128 × 17 × 2 × 2 = 8704 ch
support & cabling	410~426		
argon vessel	426~433		total 83456 ch
vacuum vessel	443~450		

Table 11-b. Parameters of Endcap LAr calorimeter

name	z (cm)	Nlayer×(Ar+Pb) in mm	# of channels
vacuum vessel wall	400~408		
argon vessel wall	410~413		N_{cell} × Interleaved
preamp & cabling	413~415		
EM layer # 1	421~426	12×(2+3)	2160 × 1= 2160 ch
EM layer # 2	426~431	12×(2+3)	8640 × 1= 8640 ch
EM layer # 3	431~444	20×(2+3)	2160 × 1= 2160ch
Hadron layer #1	444~495	62×(2+6)	2960 × 2 = 5920 ch
Hadron layer #2	495~545	62×(2+6)	2736 × 2 = 5472 ch
support & cabling	545~560		
Hadron layer #3	560~610	62×(2+6)	2528 × 2 = 5056 ch
Hadron layer #4	610~660	62×(2+6)	2160 × 2 = 4320 ch
support & cabling	660~675		
argon vessel	675~685		
vacuum vessel	690~700		
Hadron layer #0	421~444	28×(2+6)	1040 × 2 = 2080 ch
			total 35808 ch/endcap

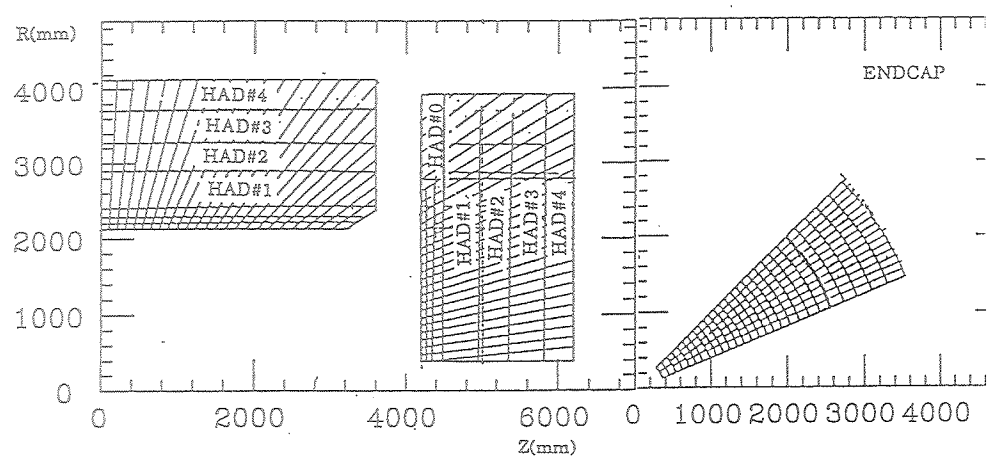

Fig.27 Layout of the Liquid Argon calorimeter

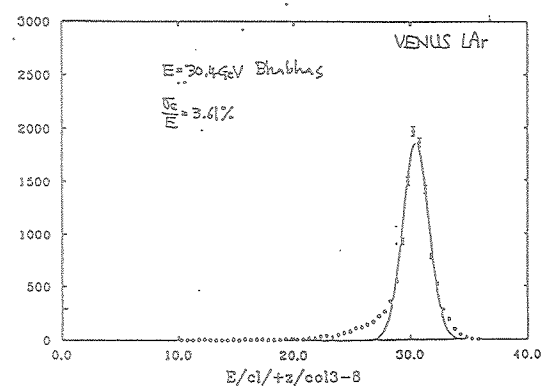

Fig.28 Energy distribution of the Bhabha events at 30 GeV observed by the VENUS LAr endcap calorimeter.

constant. This was realized by combination of minimizing noise pickup and careful works on each electronic component as described in detail in Ref [36]. This experience suggest us that if one can control the gain of each electronics channel, there remains no more ambiguity in energy determination except a single overall normalization constant. This is one of clear advantages of LAr in contrast to any calorimeter system employing optical transmission technique.

7.3 Wave form simulation [37]

We have simulated time sequence of signals from a calorimeter unit of $\Delta\eta \times \Delta\phi = 0.2 \times 0.2$ (typical hadronic shower size) at 90°. As shown in Fig.29, either bipolar or three-lobe shaping[33] is assumed with a triangle charge collection in the simulation. Minimum bias events are generated by PYTHIA with a Poisson distribution of 1.5 per bucket of 15 ns interval. A high p_t event is superimposed on these background events. We have not superimposed, however, the electronics noise yet. Simulated pulses from calorimeter units are digitized by a 60 MHz sampling ADC after proper shaping. For the time being, the highest 3 points are used to get timing and pulse height analysis as shown in Fig.30. By this simple digitization and fitting method, for a 10GeV energy deposit, one is able to determine the timing within ±1ns and pulse height within ±5% as shown in Fig.31. Table 13 summarizes the results for several other cases. It is clear from the table that it is better to use the shaping time of 50 ns rather than 100 ns. Also bipolar(n=2) or three-lobe(n=3) is less sensitive to pile-up effects. It is believed that use of faster charge collection, e.g. Argon + 0.25% Methane (t_d=200nsec) will also improve the S/N ratio, but the present simulation resulted in no difference for pile-up.

7.4 The e/h ratio

Why must the e/h ratio be close to 1? If so, how close? No colliding beam detectors so far have compensating calorimeters and they have been issuing

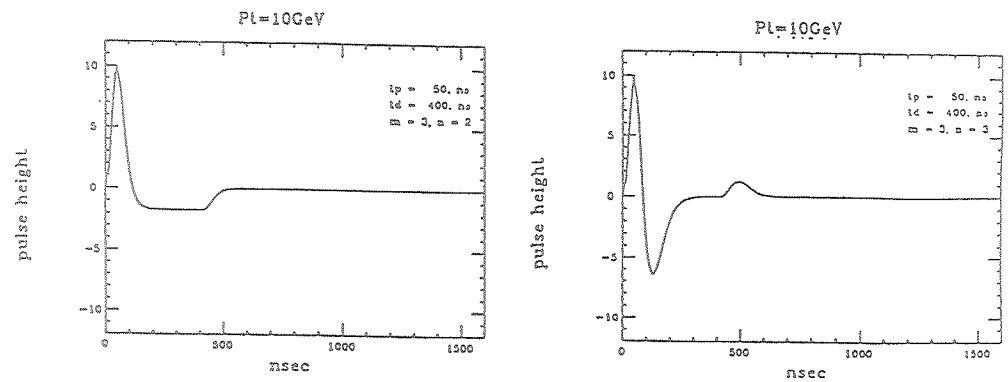

Fig.29 Wave forms used in the simulation for 10 GeV particles for the case of t_p=50ns and t_d=400ns with m=3 and (a) n=2 (bipolar) and (b) n=3 (three-lobe).

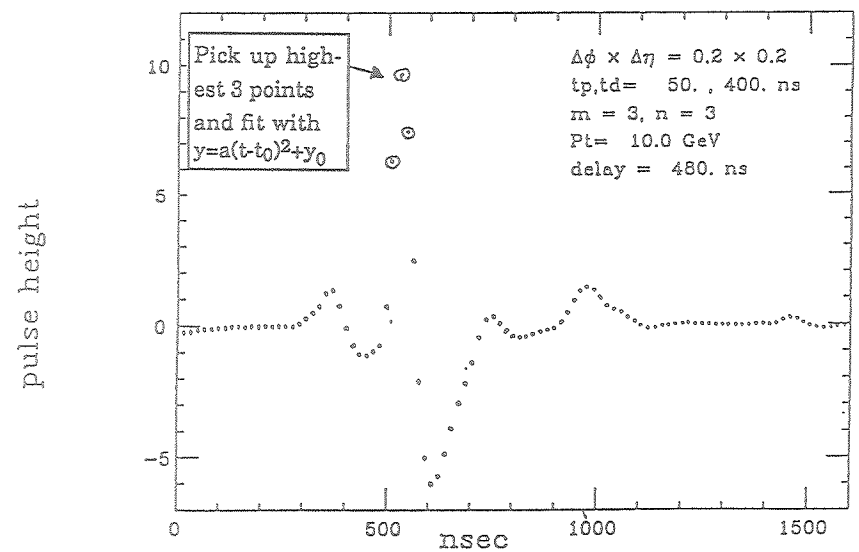

Fig.30 A simulated wave form for a 10GeV jet associated with minimum bias background observed in a calorimeter unit of 0.2 x 0.2. The analog signal is digitized by a 60MHz ADC as shown by dots.

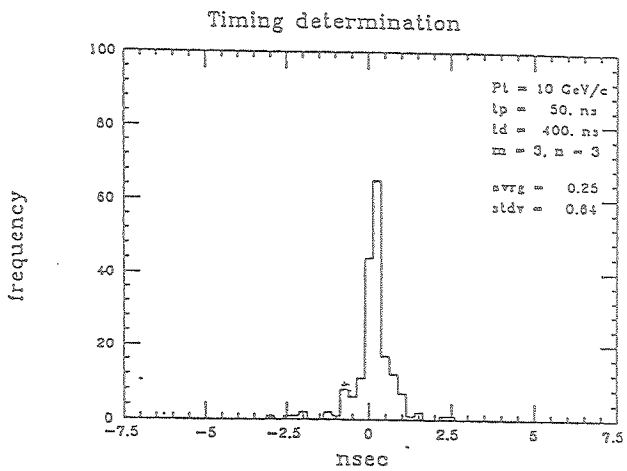

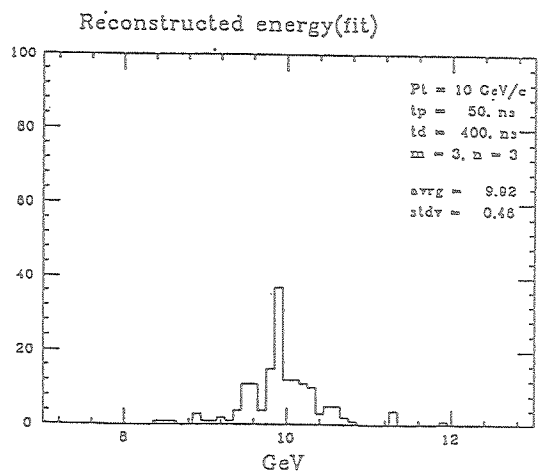

Fig.31 Time distribution and pulse height distribution for simulated 10 GeV events.

Table 12. Typical detector capacitances.

	tower names	$\eta = 0$	$\eta = 1.0$
Barrel	EM #1	0.77 nF	1.19 nF
	EM #2	0.20 nF	0.31 nF
	EM #3	2.2 nF	3.4 nF
	Had #1,#2	8.6 nF	13.2 nF
	Had #3,#4	14.3 nF	22.1 nF
Endcap	EM #3	2.23 nF	
	Had #1,2	24.8 nF	
	Had #3,4	34.4 nF	

Table 13. Results of pile-up effects in pulse simulation of LAr.

t_p nsec	t_d nsec	m	n	E_0 GeV	Δt nsec	σ_t nsec	ΔE GeV	σ_E GeV
50	400	3	1	10	-0.70	3.25	0.82	0.81
50	400	3	2	10	1.84	0.61	-0.02	0.42
50	400	3	3	10	0.25	0.64	-0.08	0.46
100	400	3	1	10	-1.13	3.17	1.08	0.70
100	400	3	2	10	0.79	1.89	-0.15	0.60
100	400	3	3	10	0.0	1.91	-0.06	0.70
50	200	3	3	10	0.14	1.40	-0.05	0.90
50	400	3	3	10	0.25	0.64	-0.08	0.46
50	400	3	3	10	0.25	0.64	-0.08	0.46
50	400	3	3	100	0.19	0.12	-0.82	0.47

where t_p = peaking time, t_d = charge carrier drift time,
m=# of integration(RC), n = # of differentiation(CR),
E_0 = input energy into calorimeter,
Δt and σ_t = reconstructed timeing (deviation and rms).
ΔE and σ_E = reconstructed energy (deviation and rms).

good physics (e.g. CDF). The reasons for unit e/h ratio are (1) smaller constant term in energy resolution and (2) more linear energy response. As for the energy resolution, it is a general consensus that high p_t physics do not require super energy resolution[38]. Even $1.0/\sqrt{E(GeV)}$ is good enough for physics even if systematic effects are small. At high energies, calibration is of major concern rather than resolution. In this respect, the energy non-linearity caused by e/h≠1 is quite serious, faking compositeness of quarks in jet p_t spectrum for example[39].

It is known that the e/h ratio can be adjusted to be 1 by using high Z materials as absorbers and low Z as active materials with appropriate thickness and by using active materials including hydrogen atoms[40]. However the gap between these requirements and practical technology for construction of calorimeters seems to be still large. We have investigated two ways to effectively obtain unit e/h ratios.

The H1 detector has lead EM and iron hadron LAr calorimeters. They used so-called weighting method developed by CDHS and obtained reasonable energy resolution[41]. In our simulation using GEANT, assuming 4 depth segmentations, the method worked at higher energy of ~500 GeV, but did marginally at lower energy, probably due to too few depth division[42].

Effects on non-unit e/h ratios on the energy resolution were investigated by Monte Carlo simulation for 50GeV and 1TeV jets[43]. Jets are generated by LUND6.3 and an energy dependent e/h ratio is assumed[44]. Figs.32a and 32b indicate that the energy resolution of jets are less e/h dependent. Since we have at least two (EM and hadron) depth segmentations in the calorimeter, we may correct the response of the calorimeter for hadrons using the observed R_{EM}=EM/TOT ratios. In the simulation, we used parametrization given by Bock for longitudinal shower development. Fig.33a show two dimensional plots of total observed energy vs the observed ratio R_{EM} for 50GeV jets for the case of e/h (at 1GeV) of 1.4. One sees a rather clear trend, constant up to R_{EM} ~0.55 and

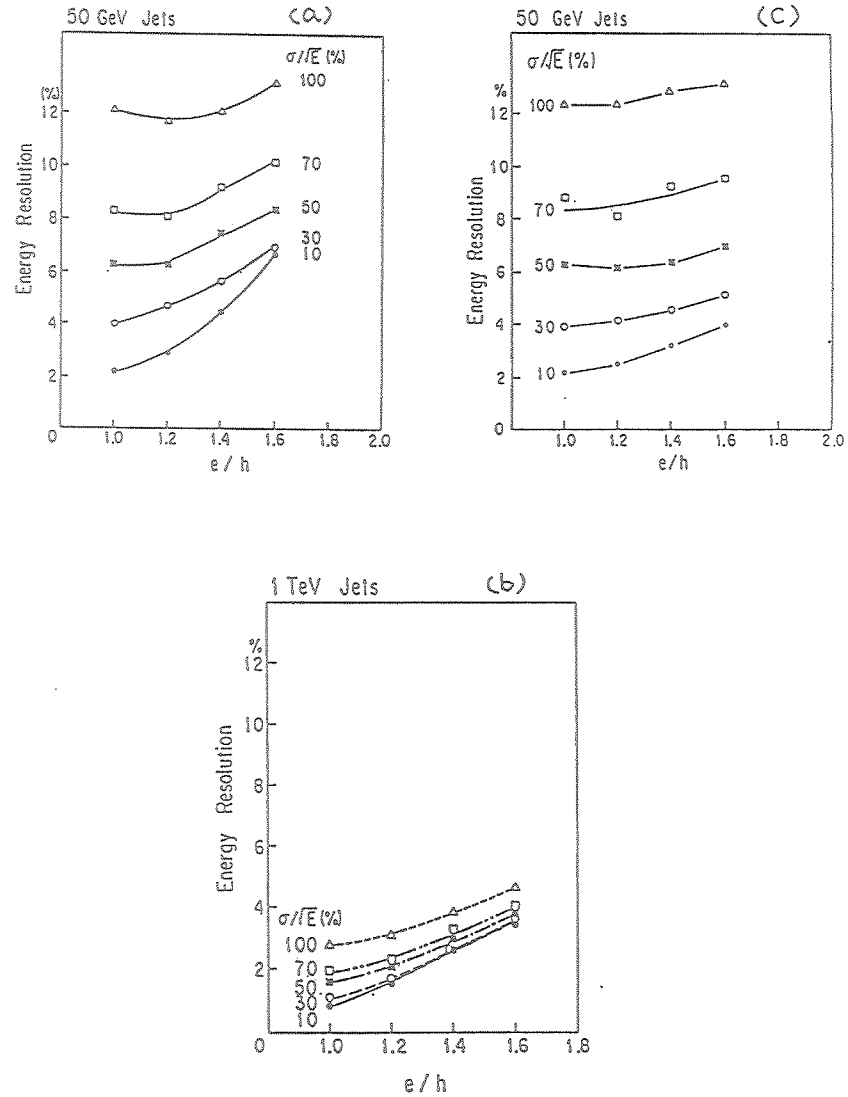

Fig.32 Energy resolutions for (a) 50GeV jets, (b) 1 TeV jets and (c) 50GeV jets with the R_{EM} correction, as a function of R_0, the e/h ratio at 1GeV, for various intrinsic hadron resolutions.

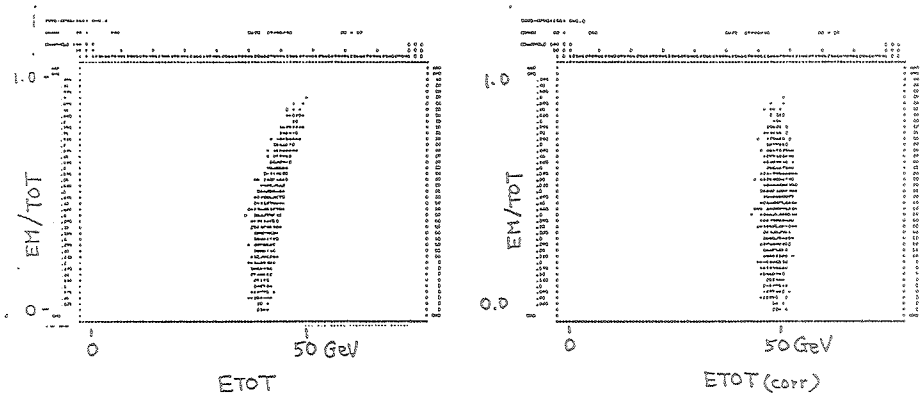

Fig.33 Two-dimensional plot of the total observed energy vs observed EM/TOT for 50 GeV jets in the case of $R_0 = 1.4$ before (a) and after (b) the corrections.

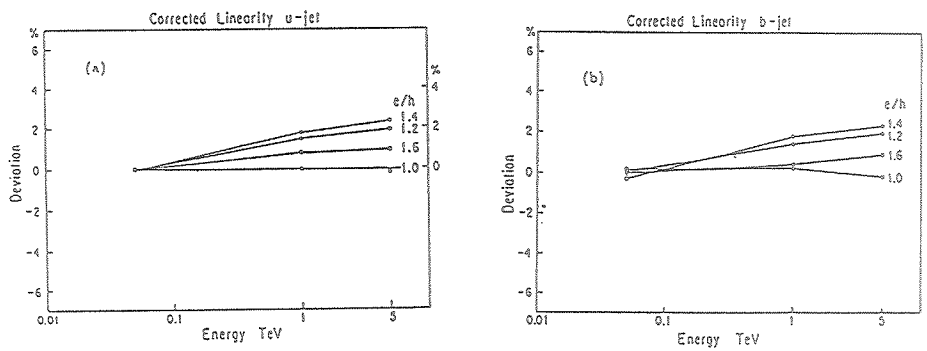

Fig.34 Deviation in linearity of the response of a calorimeter for (a) u-jets and (b) b-jets, where non-linearities are corrected by the response of u-jet. The u-jet curve should show exactly 1.0 but we stopped calculation before the correction function used becomes ideal. But the essence of this correction is clear.

linear relation up to 1.0. By knowing this trend, one can make a energy correction by using observed quantities only, as shown in Fig.33b. With this correction applied, we are not suffered any more from degradation in jet energy resolution even at 50GeV as shown in Fig.32c. The energy non-linearity, however, cannot be corrected in the same manner, unless one knows the energy dependence of the e/h ratio of the calorimeter in use. With known e/h behavior, one can obtain the correction factor to energy non-lineality using simulated jets. In order to check the validity of this procedure, we applied the non-linearity correction function obtained by simulated u-quark jets to b-quark jets. The difference, as shown in Fig.34, was less than 1% for whole energy region. This kind of correction to non-linearity can be checked by using, for example, the method of direct γE_t balancing developed by CDF[45].

In summary, as far as jet energy measurement is concerned, there seems no reasons to require the e/h ratio close to 1.0. There are number of ways to perform resolution and linearity corrections to the level sufficient enough for high p_t physics we are aiming. This is one of the reasons why we think use of lead as the calorimeter absorber is adequate.

7.5 Preamplifiers in the liquid

It is proposed to place the preamplifiers directly at detector electrodes to improve charge collection speed[33]. The preamplifiers must be submerged in the liquid as in Helios. Charge amplifiers with JFET has been developed for this purpose. Preamplifiers must be radiation resistant in this configuration. We are investigating a possibility of using one of GaAs FET's called HEMT (high electron mobility transistor) developed by Fujitsu. Among many attractive features, the device works better at cryogenic environment and there is an evidence of radiation resistance up to 100Mrads(γ). Fig.35 illustrates a readout scheme under consideration. HEMT preamplifiers of Gilbert type are located in the liquid, while differential charge amplifiers are placed outside the

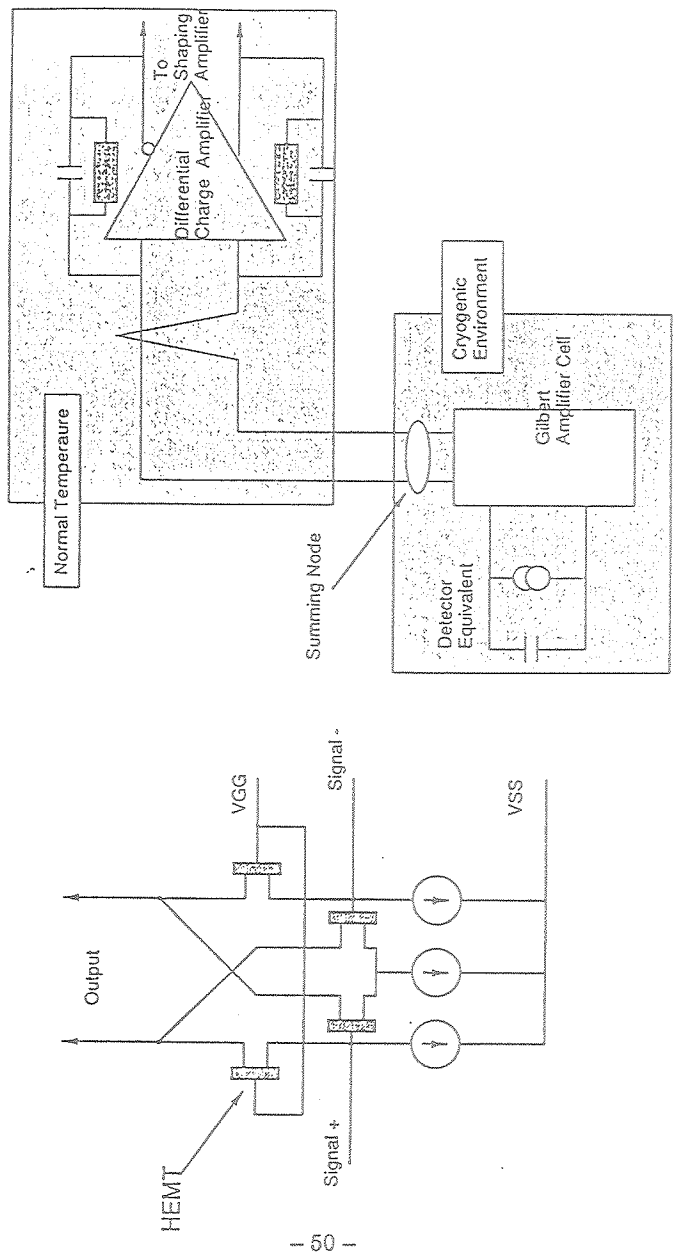

Fig.35 Readout scheme of LAr calorimeter using HEMT Gilbert amplifiers.

cryostat. The Gilbert amplifier offers stable operation for wide range of temperature. In this scheme, the summing node is free from disturbance of detector capacitances so that quick charge collection is practical. High capacitance of detector is not seen by the charge integrating amplifier. It may be compatible with differential readout of electrostatic transformer scheme.

8. Inner Tracking System

8.1 Hit rates

It has been pointed out that the charged particle flux from minimum bias events are extremely high and close to the operational limit of wire cambers[46]. Thus solid angle covered by one cell must be considerably reduced for operation. The number of wires becomes large as a consequence. An idea of a straw tube system was introduced in 1986 Snowmass[47]. It has been also pointed out that, under solenoid field, low p_t particles generate curling trajectories and thus increase the radiation level as well as the average hit rate[48]. We have calculated hit rates of charged particles including γ conversions by chamber material using GEANT for various field strength[49]. Fig.36 shows the case for 2T field for straws of 5mm in diameter covering four different rapidity ranges. As shown, curling tracks double the hit rate at the radius between 50 and 100cm. Table 14 summarizes results of the dependence on field strength. One notices that there are little differences between hit rates at 1T and 2T. Also no field dependence is seen at outer radius (150cm).

8.2 Wave form simulation

Effects of noise and signal wave forms were evaluated for straw chambers[50]. In case of long straws, an effect from series noise becomes significant for short shaping time. In our simple model for simulation, the ionization along a track is uniform, the drift velocities of both electrons and ions are constant, the

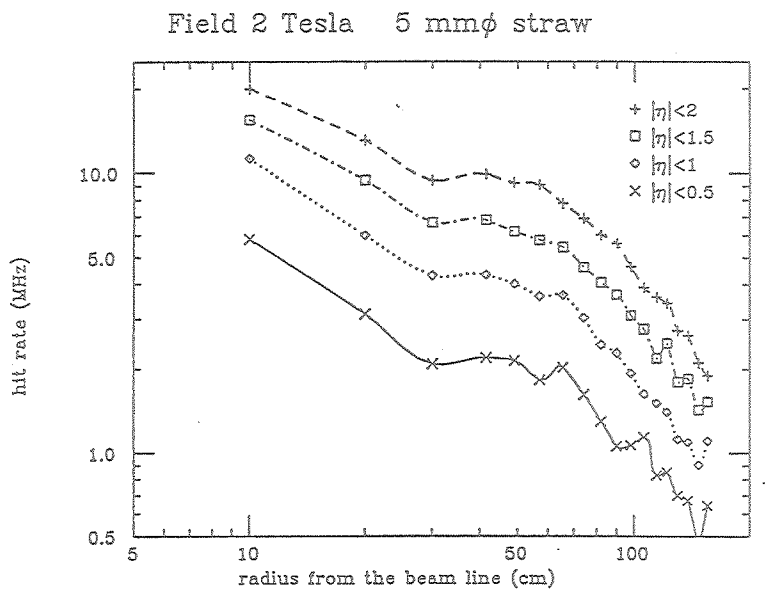

Fig.36 Charged particle hit rates in 5mm straws covering 4 different rapidity ranges. The solenoidal field of 2 Tesla is assumed.

Table 14. Hit rate of straw(5 mm in diameter) tubes .

Rapidity Coverage		|η|< 1			|η|< 1.5			|η|< 2		
radius	cm	50	100	150	50	100	150	50	100	150
length of straw	cm	117	235	353	213	423	639	363	725	1088
hit rate (B=0T)	MHz	2.3	1.2	1.0	3.2	2.0	1.5	4.5	2.4	2.1
hit rate (B=1T)	MHz	2.7	2.1	1.3	4.1	3.1	1.7	6.5	4.7	2.4
hit rate (B=2T)	MHz	4.0	1.9	1.0	6.2	3.1	1.5	9.2	4.6	2.0

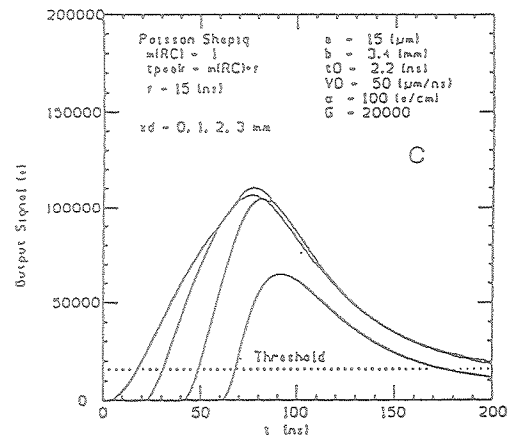

Fig.37 Simulated pulse shapes of straw chambers for four different crossing points (0,1,2,3mm from the sense wire). The shaping time is 15ns[50].

Table 15. Central tracking system with straw tubes, old and new.

items	Berkeley 87	present design	limit (?)
No. of superlayers	15	4	
No. of Z segment	1	3	
layers / superlayer	8	8	
No. of straws	1.22×10^5	1.15×10^5	
Inner radius	40 ~ 152 cm	105 ~ 155 cm	
rapidity coverage	1.23	1.4	
straw diameter	3.9 ~ 6.8 mm	6.4 ~ 7.3 mm	
straw length	1.7 ~ 4.8 m	1.6 ~ 2.2 m	
gas gain	2×10^4	10^5	
current/wire	0.5 μA	0.35 μA	< 1 μA
collected charge	0.12 C/cm/5 yrs	0.09 C/cm/5 yrs	< 1C/cm
hit rate (B=2T)	3 MHz	1 MHz	< 1 MHz
detector capacitance	50 pF	20 pF	
ENC	~ 3900 e	~1800 e	
time jitter	~ 4 ns	~ 0.4 ns	< 1ns
time walk	~ 12 ns	~ 1 ns	< 1ns

avalanche occurs at the surface of the anode wire with the constant gas gain, and the tube chambers is treated as a single capacitance for the analysis of the signal processing. If the drift time is determined by the threshold-crossing method, the threshold must be set at about five times the noise level. Then it turned out that the gas gain of ~10^5 is necessary for a 5m long tube to get the position resolution of 150μm. Necessary gas gain is roughly proportional to the tube length L for $2 < L < 5$ m, and 4×10^4 for $L < 2$m. The time constant of τ = 10~15ns seems to be optimum value from a viewpoint of the time resolution and the pileup problem. As shown in Fig.37, even with this short time constant and even if the 1/t tail is cancelled, it would take roughly about 100ns to be ready for the next pulse.

8.3 Hybrid tracker system[66]

Two studies described above, on the hit rate and on the signal processing, indicate us that straw tubes longer than 2m would encounter serious difficulties in their operation at the luminosity of $10^{33}cm^{-2}s^{-1}$. Our compromise on the straw tubes is

	rather short tube L :	≤ 2m
	hit rate :	≤ 1 MHz
	gas gain :	≈ 10^5
	number of sense wires :	≈ 100 K (for barrel).

The last requirement is somewhat arbitrary but we think reasonable. Now how to adapt these new operational/hardware requirements to the design of tracking system? Table 15 lists changes we propose on the relevant parameters from the 87 Berkeley LSD design[6].

Now we propose here a hybrid tracking system associated with the change of tracking concept. At present, there seems no single technology that can cover the entire tracking volume with three-fold capabilities required for the tracking system, i.e. (1) accurate position measurement,

(2) pattern recognition

and (3) ton-line triggering.

Wires (straws) can not be reliable enough in the region of small radii. On the other hand, a silicon strip system can only be fit to small radii. Since position resolution by silicon strips is far better, it is reasonable to rely on silicon system for momentum determination[51]. On the other hand, silicon strips are not so great in triggering and pattern recognition. The superlayer system of straw tubes is best suited for these two functions. A track pattern recognized in the outer straw tubes can be extrapolated inward to pick up corresponding hits on silicon strips to form a single track. For this function-separated hybrid system, our guess for optimal dividing line is around r=100 cm instead of usual 50 cm. Thus we propose :

r = 10 ~ 90 cm :	silicon strip system :	momentum determination
r = 100 ~160 cm :	straw tube system :	pattern recognition & triggering

The proposed hybrid system are sketched in Fig.38.

8.4 Straw tube system

Table 16 shows relevant parameters of the central straw tracking system. Four superlayers (32 hits along the trajectory) seem adequate for initiating the track pattern recognition. The central and left/right layers overlaps at their edges to avoid dead regions. We propose use of the TMC circuit for digital time readout on the chamber as described later. Z coordinate will be obtained by measuring the time difference of pulses from both ends of straw tubes. Therefore number of readout channels is twice of straw tubes.

The forward region of rapidities between 1.5 and 2.5 will be covered with the same type of straw tubes in order to minimize the hit rate per sense wire and to avoid complexities due to such as field wires or field shaping cathode strips. Just like the barrel trackers, 8 layers of straws make a superlayers for easy pattern recognition. Twelve superlayers (96 hits) per side seem to be reasonable for recognition of tracks. As shown in Fig.39 and Table 17, the superlayers will

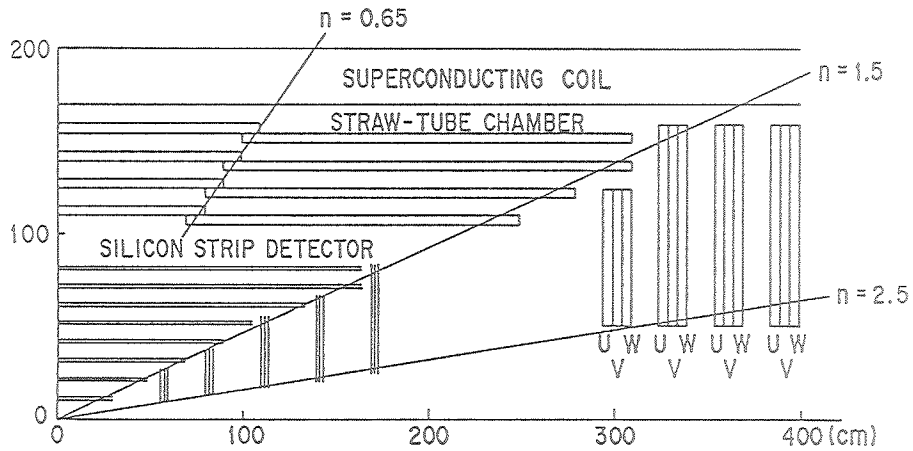

Fig.38 Hybrid system of the inner tracking detectors.

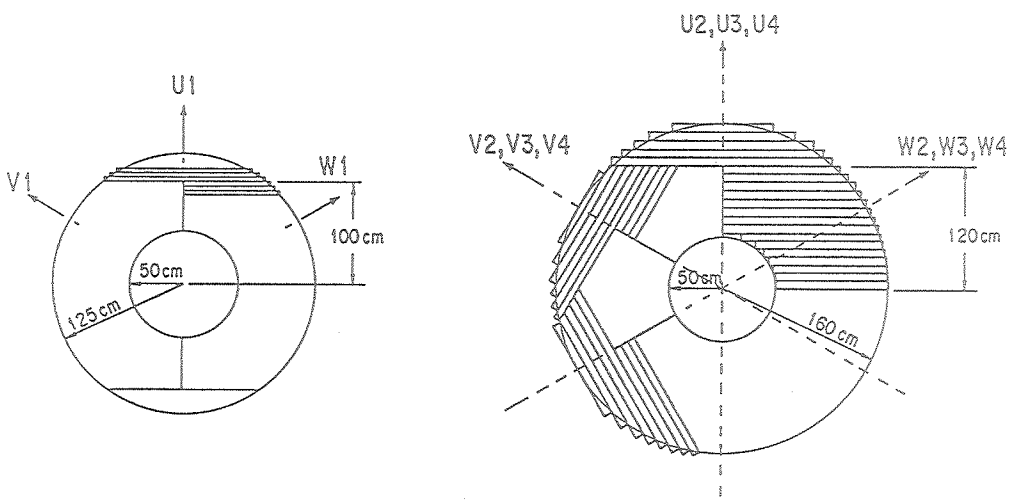

Fig.39 A sketch of the forward straw tube system.

Table 16. Parameters of the straw tube tracking system

Superlayer #	radius	length	diameter	rapidity	N(straw)	readout ch
C 1	110 cm	160 cm	7.0 mm	-0.65~+0.65	8256	16512
C 2	125	180	7.0	-0.65~+0.65	9328	18656
C 3	140	200	7.25	-0.65~+0.65	9696	19392
C 4	155	220	7.23	-0.65~+0.65	10768	21536
LR 1	105	180	6.4	±(0.65~1.5)	8256 × 2	33024
LR 2	120	200	6.4	±(0.65~1.5)	9328 × 2	37312
LR 3	135	220	7.0	±(0.65~1.5)	9696 × 2	38784
LR 4	150	210	7.0	±(0.65~1.4)	10768 × 2	43072
					Total number of straws =	114144
					Total number of readout channels =	228228

Table 17. Parameters of straw-tube tracking system

superlayer number	z position	radial position	straw length	straw diameter	rapidity range	No. of straws	No. of readout
U1	2.95 m	50~125 cm	75~150 cm	7 mm	1.64~2.45	5140	5140
V1	3.00	50~125	75~150	7	1.64~2.45	5140	5140
W1	3.05	50~125	75~150	7	1.64~2.45	5140	5140
U2	3.25	50~160	105~210	7	1.50~2.50	6394	6394
V2	3.30	50~160	105~210	7	1.50~2.50	6394	6394
W2	3.35	50~160	105~210	7	1.50~2.50	6394	6394
U3	3.55	50~160	105~210	7	1.50~2.55	6394	6394
V3	3.60	50~160	105~210	7	1.50~2.55	6394	6394
W3	3.65	50~160	105~210	7	1.50~2.55	6394	6394
U4	3.85	50~160	105~210	7	1.64~2.65	6394	6394
V4	3.90	50~160	105~210	7	1.64~2.65	6394	6394
W4	3.95	50~160	105~210	7	1.64~2.65	6394	6394
Total number of readout channel (for each endcap) =							72966

Table 18. Parameters of Silicon Strip Tracking System (Barrel Part)

radial position	strip pitch	expected resolution	strip length	No.of z segmts	readout strip pitch	strip capacitance	No.of pieces ϕ x z = total	No.of readout ch
cm	μm	μm	cm		μm	pF		x 10^3
10	25	7.5	20	3	75	5	12 x 9 = 108	30.7
12	25	7.5	20	3	75	5	12 x 9 = 108	30.7
20	25	7.5	20	5	75	5	22 x 15 = 330	93.9
22	25	7.5	20	5	75	5	22 x 15 = 330	93.9
30	50	15	20	7	100	7	32 x 21 = 672	143.4
32	50	15	20	7	100	7	32 x 21 = 672	143.4
40	50	15	20	9	100	7	42 x 27 = 1134	241.9
42	50	15	20	9	100	7	42 x 27 = 1134	241.9
50	50	15	30	7	100	10	52 x 35 = 1820	233.0
52	50	15	30	7	100	10	52 x 35 = 1820	233.0
60	100	30	30	9	200	20	62 x 45 = 2790	178.6
62	100	30	30	9	200	20	62 x 45 = 2790	178.6
70	100	30	30	11	200	20	72 x 55 = 3960	253.4
72	100	30	30	11	200	20	72 x 55 = 3960	253.4
80	100	30	30	11	200	20	82 x 55 = 4510	288.6
82	100	30	30	11	200	20	82 x 55 = 4510	288.6
total number of detector pieces = 30648								
total number of readout channels = 2.93 x 10^6								

Table 19. Parameters of Silicon Strip Tracking System (Endcap Part)

z position	radial position	strip pitch (radian)	strip capacitance	No.of strips	readout pitch (rad)	No.of readout chanl front	back
56 cm	10-28 cm	0.25 x 10^{-3}	4 pF	25120	0.5 x 10^{-3}	12560	6280
58	10-28	0.25	4	25120	0.5	12560	6280
60	10-28	0.25	4	25120	0.5	12560	6280
80	13-38	0.25	8	25120	0.5	12560	6280
82	13-38	0.25	8	25120	0.5	12560	6280
84	13-38	0.25	8	25120	0.5	12560	6280
110	18-35	0.25	6	25120	0.5	12560	6280
	35-55	0.25	10	25120	0.5	12560	8374
112	18-35	0.25	6	25120	0.5	12560	6280
	35-55	0.25	10	25120	0.5	12560	8374
114	18-35	0.25	6	25120	0.5	12560	6280
	35-55	0.25	10	25120	0.5	12560	8374
140	21-46	0.25	10	25120	0.5	12560	8374
	46-66	0.25	13	25120	0.5	12560	8374
142	21-46	0.25	10	25120	0.5	12560	8374
	46-66	0.25	13	25120	0.5	12560	8374
144	21-46	0.25	10	25120	0.5	12560	8374
	46-66	0.25	13	25120	0.5	12560	8374
170	25-45	0.25	8	25120	0.5	12560	6280
	45-65	0.25	13	25120	0.5	12560	8374
	65-85	0.25	18	25120	0.25	25120	16748
172	25-45	0.25	8	25120	0.5	12560	6280
	45-65	0.25	13	25120	0.5	12560	8374
	65-85	0.25	18	25120	0.25	25120	16748
174	25-45	0.25	8	25120	0.5	12560	6280
	45-65	0.25	13	25120	0.5	12560	8374
	65-85	0.25	18	25120	0.25	25120	16748
Total number of readout channels for each endcap Front plane = 376800 Back plane = 226092							

be rotated by 120° forming X,U and V planes for stereo reconstruction. The signal readout is from one side of a straw for this case.

8.5 Silicon strip detectors

There are two obvious advantages, low hit rate per channel and superb position accuracy in a silicon strip system. It has been used for many high energy experiments for last ten years and therefore it is one of established technologies, leaving us no fundamental problems but engineering issues. Radiation damage in detector and associated electronics is one of the critical issues for application to the SSC. Radiation effects of silicon detector have been studied for charged particles[52], neutrons[53] and γ-rays[54]. Total dose increases leakage current and changes the pulse height as well as operation voltage. Leakage current will degrade the S/N ratio due to shot noise. The shot noise can be reduced with fast shaping time[55]. Radiation damage in bipolar and radiation hardened CMOS technology have been studied[56]. There exist accumulation of rad-hard technology by number of companies in USA[57].

Power consumption is one of major concerns. If we use one of ultra fast bipolar processes (for example SST by NTT), it may take ~7 mW/channel for digital (on/off) readout with 20 ns shaping time[58]. 4.2 million readout channels as proposed here correspond to 30kW power dissipation. Clearly we need reasonable compromise among speed, S/N, capacitance and number of channels. Tables 18 and 19 are parameters of the proposed silicon strip systems of barrel and endcap part. The design is based on minimizing number of readout channels. The unit size of a silicon microstrip detector assumed is 6.4x6.4cm^2 corresponding to a 4-inch wafer. The strip pitch gets larger for higher radius. We apply the charge division technique associated with digital readout scheme[59]. Three or five strips along z direction will be connected by bonding to one readout channel. For the endcap strip system, double sided strips under R&D will be used.

8.6 Momentum resolution

Fig.40 shows the momentum resolution at 90°. Multiple scattering dominates up to 50 GeV/c but we obtain excellent resolution of 15% at 1 TeV. This is more than enough for Heavy H → 4μ and adequate for new Z search up to 2 TeV.

8.7 Non-uniform magnetic field

What is the effect of non-uniform magnetic field due to the air-core configuration of the solenoid? The uniformity of field is not essential for tracking. This has been proved in several experiments. AMY has ~20% variation of field strength in their drift chamber region, but by iteration, they achieved good momentum resolution. Br and Bz are plotted in r-z plane in Fig.41. As one goes to higher rapidity, the integral Bdl (B x dl) becomes smaller as shown in Fig.42. ZEUS has a graded coil winding to achieve better field uniformity by increasing ampere-turns at the coil end[11]. This is for future study.

8.8 TMC

Time memory cell (TMC) is a proposal of time measurement system for high intensity collider experiments [60]. TMC directly digitizes and memorize timing of pulses without invoking analog circuits as is shown in Fig.43. This is in contrast to the time to voltage conversion method[61]. The principle of TMC was proven using 0.8μm CMOS technology with time resolution of 0.8nsec[62]. A complete readout system for straw tube system is described in detail elsewhere[63].

It is possible to develop a z coordinate readout by direct time measurement at the both ends of a straw tube. Although electronics channel doubles, no additional wires are needed. The z information thus obtained can be used for the 1st/2nd triggers for track-calorimeter matching. Time accuracy of 0.5ns

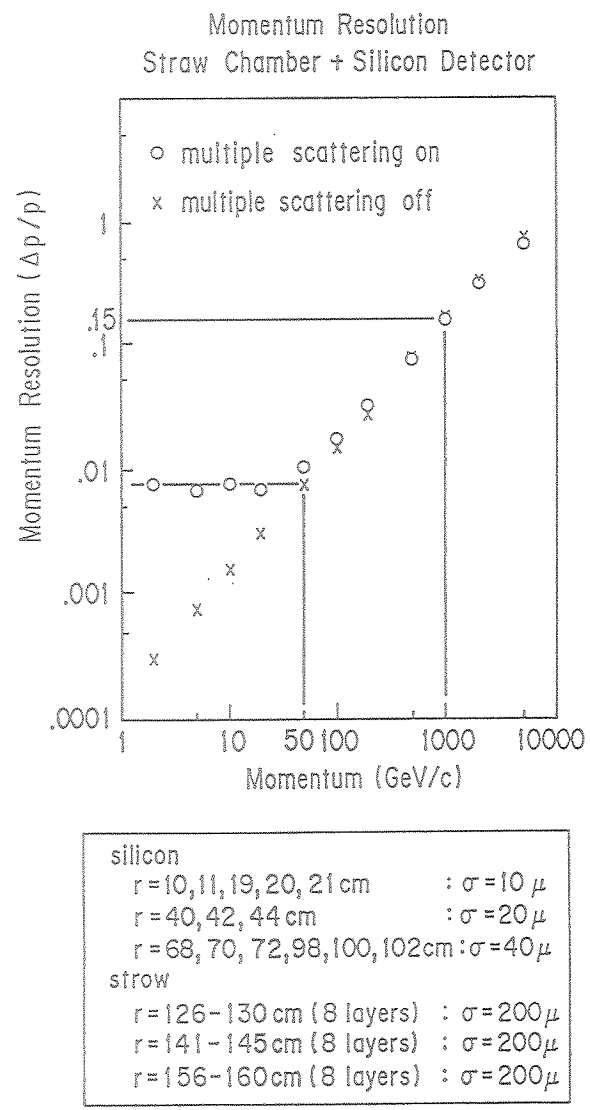

Fig.40 Momentum resolution at 90° with the hybrid silicon/straw system.

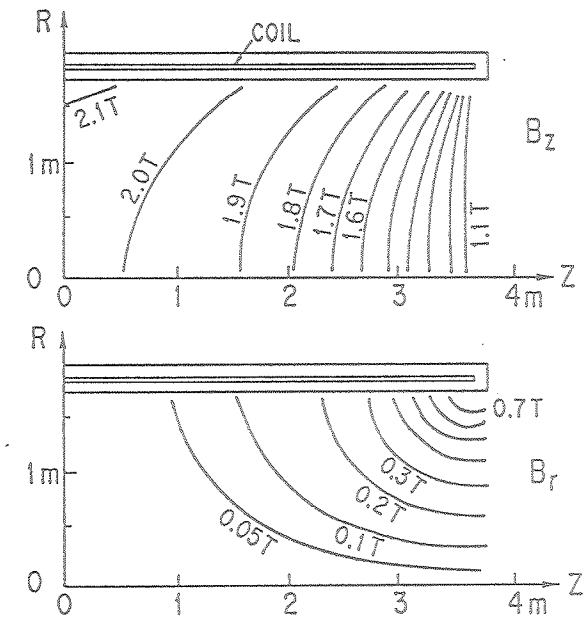

Fig.41 Contours of Br and Bz components in the central tracing region.

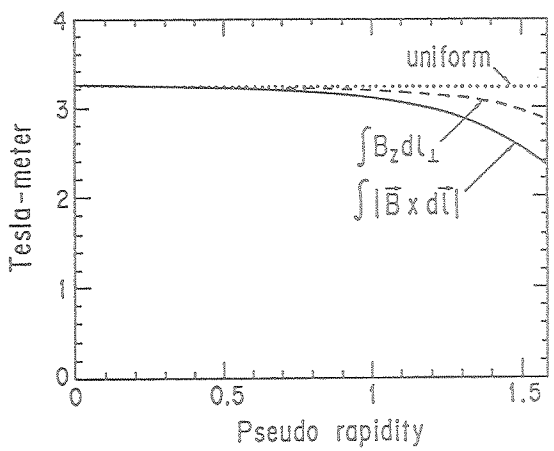

Fig.42 Integral Bdl as a function of rapidity.

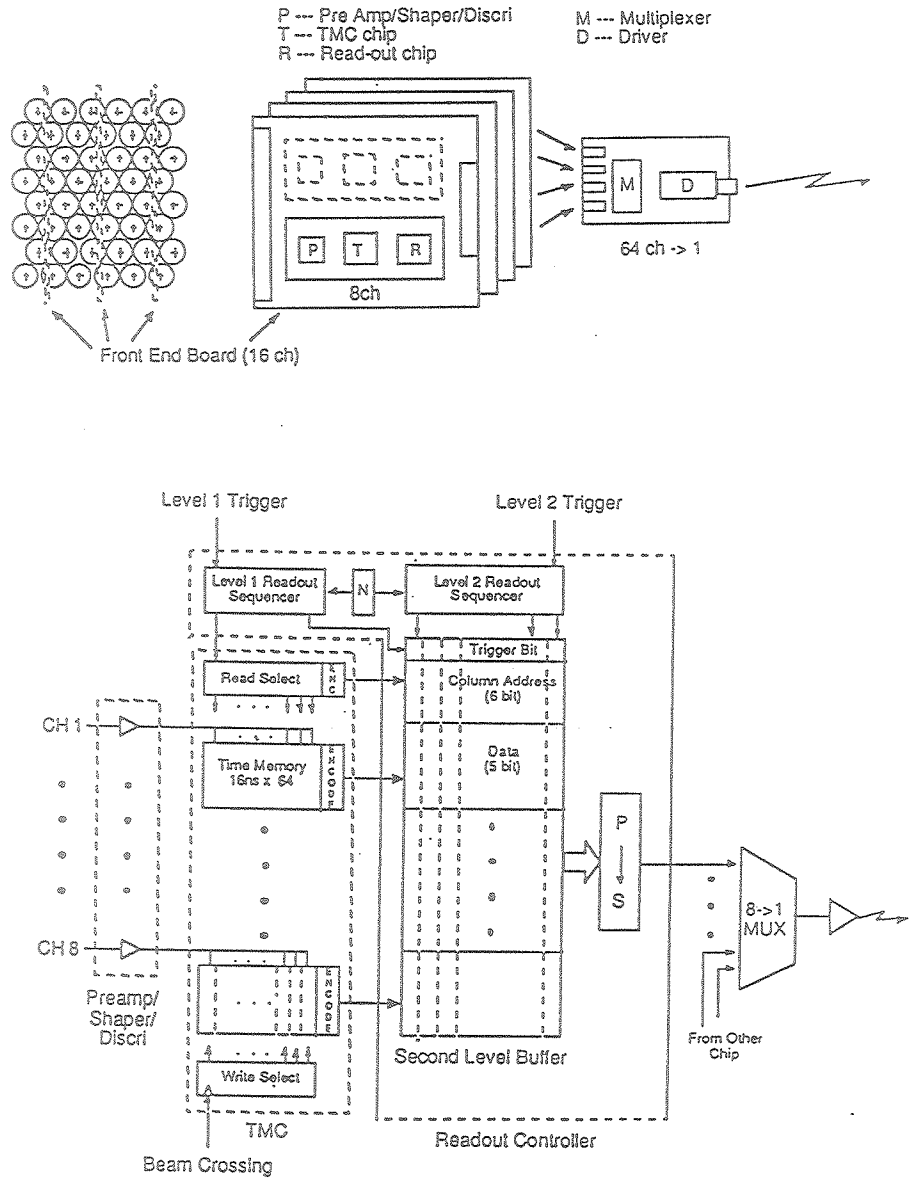

Fig.43 TMC time measurement system for straw chambers.

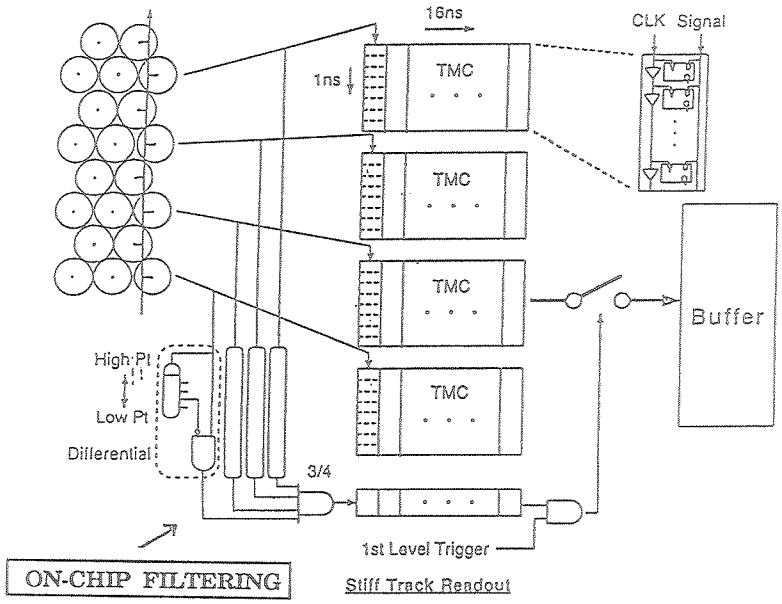

Fig.44 On-chip filtering of straw tubes readout on a TMC chip.

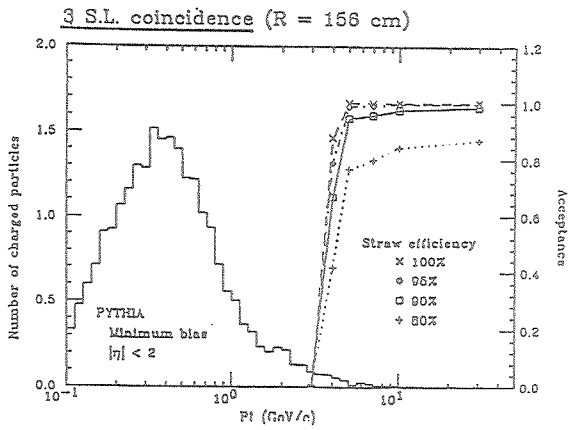

Fig.45 Efficiencies of the 3 superlayer coincidence of the 3-out-of 4 coincidences as a function of p_t for various tube efficiencies. The p_t distribution of charged particles from minimum bias events by PYTHIA is shown.

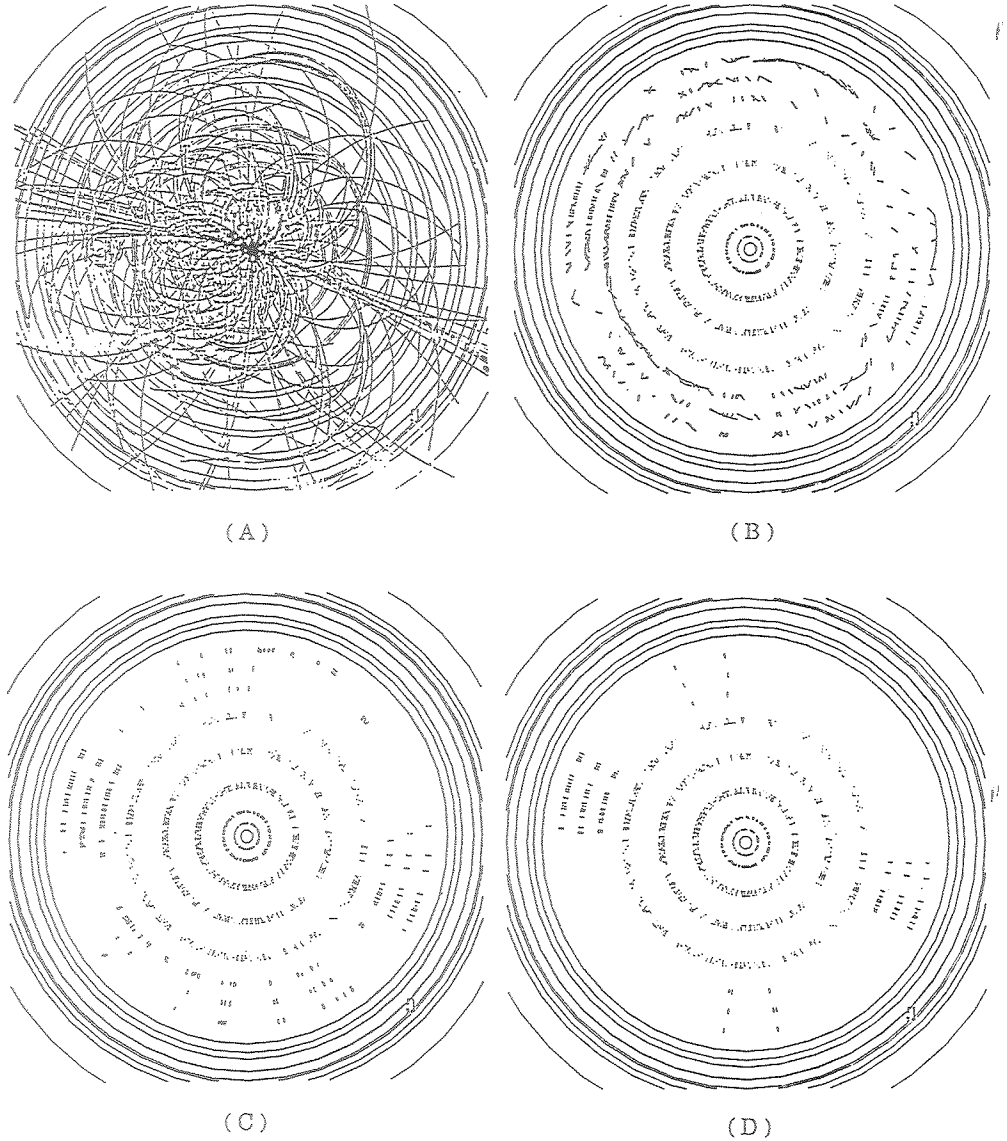

Fig.46 An example of a Higgs particle decaying into 4 muons superimposed by 5 minimum-bias events : (A) generated event, (B) hits in tracking detectors, (C) after the 3-out-of-4 coincidence in each superlayer, and (D) after the 3-fold coincidence of the 3 superlayers.

corresponds to Δz ~5 cm enough for pointing the EM tower and the silicon trackers.

8.9 On-chip filtering of low p_t tracks

Most of charged tracks have p_t less than 1 GeV/c. They are irrelevant to high p_t physics that we are pursuing. An on-chip filtering method looks possible for the straw tube system to get rid of such low p_t tracks[64]. As shown in Fig.44 we require a 3 out-of 4 coincidence of straw tubes in a superlayer. Such a coincidence can be easily realized on-chip of the TMC circuit as shown. We have calculated the efficiency of the 3/4 coincidence logic for one superlayer as well as for demanding 3 superlayer coincidence. Fig.45 shows the efficiency as a function of p_t for different straw tube efficiencies. Plotted together is the p_t distribution of minimum bias events. After the 3/4 logics applied to five overlapped minimum bias events, few tracks are left as shown in Fig.46. Thus one can expect the output of 3/4 logics would be quite useful for isolated track trigger in 2nd/3rd level triggering.

9. Conclusions

1. We propose ACS as a practical version of the Berkeley '87 LSD design with
   air-core solenoid
   barrel iron toroid
   and hybrid tracking system
   without any serious compromises in hermeticity, electron/muon detection capabilities.
2. An air-core solenoid seems to be technically feasible and be attractive in cost, time for construction, transportation, structural aspects and operation. Some engineering details and parameters are presented.

3. We propose an iron muon toroid system for both barrel and endcap region. The system provides hermetic μ detection with high μ identification and triggering capabilities. Charge of μ's can be determined for $P\mu$ ~ 2TeV.
4. We prefer liquid argon for calorimeter because of survival, stability, calibration etc. Relatively slow charge collection seems not to be a serious problem by the use of fast shaping electronics. Pulse transformers may be used for most part of calorimeter if they can work for up to B=0.5 Tesla with proper shielding. A simulation study on the e/h ratio showed no appreciable difficulty in jet energy measurements.
5. We propose a hybrid system for inner tracking detector. Silicon microstrips give excellent $\Delta P/P$, while straw tubes at large radii are very useful for pattern recognition and triggering of isolated high P_t particles.
6. As for structural consideration, by fixing barrel muon toroid in the experimental hall, the installation of and access to the rest of detector components become realistic.

Acknowledgements

I like to thank many people who contributed to the present study. I also thank T.Ohsugi and S.Mori who forced me to make this write-up. I thank A.Maki for his immediate reading of this manuscript and his kind comments.

References and Notes

[1] K.Ogawa, presented at the 5th Workshop for Hadron Collider Physics at Shinshyu, August, 1988.

[2] F.Abe, K.Amako, Y.Arai, Y.Fukui, H.Ikeda, H.Iwasaki, T.Kondo, A.Maki, K.Ogawa, Y.Sakai, Y.Takaiwa, S.Terada, N.Ujiie, Y.Unno, Y.Watase, A.Yamamoto (KEK), Y.Asano (Tsukuba U), Y.Watanabe (Tokyo Inst. Tech.), S.Sugimoto (Osaka U), N.Tamura (Okayama U), T.Ohsugi (Hiroshima U), M.Asai(Hiroshima Inst. Tech.) and many others.

[3] Workshop on Experiments, Detectors, and Experimental Areas for the Supercollider, July 7-17, 1987, Berkeley.

[4] D.Groom, Snowmass 88, p711, and Report of the Task Force on Radiation Levels in the SSC Interaction Regions, SSC-SR-1033, June 1988.

[5] H.H.Williams, Talk presented at the Workshop of SDE, Dallas, June 25-29, 1989.

[6] G.G.Hanson et al., Report of the Large Solenoid Detector Group, Proceedings of the Berkeley Workshop, July 1987, pp.340-387.

[7] S.Mori, Conceptual design studies of large solenoids, JSD-Note-1990-7.

[8] R.W Fast et al., Proceedings of the Summer Study on High Energy Physics in the 1990s, Snowmass, 1988, p841, and S.Mori, ibid. p837.

[9] E.Wang, Talk presented at the Calorimeter Workshop at Tuscaloosa, March, 1989.

[10] See pp.449-453 in the Proceedings of the 1987 Berkeley Workshop.

[11] The ZEUS Detector: Technical Proposal, March 1986, and Status Report , March 1989.

[12] M.Derrick, Proceedings of the Summer Study on High Energy Physics in the 1990s, Snowmass, 1988, p791. It is interesting to quote one of his statements from this article :

" A perfect detector like a perfect spouse exists only in dreams; reality imposes some compromises. However, the detector design must be driven by the principal physics goals and not by technological hubris. To overstate the case, one should try to always use obsolete technology."

[13] R.Fast et al., Fermilab Report TM-1135, 1982.
H.Minemura et al., Nucl. Instr. and Methods, A238(1985)18.

[14] A.Yamamoto et al., Jpn. J. Appl. Phys. Lett., 25(1986)L440.

[15] M.Wake et al., IEEE Trans. on Magnetics, MAG-21(1985)494.

[16] Y.Makita et al., to be published in the proceedings of the 11-th Int. Conf. on Magnet Technology, KEK-Preprint 89-147 (1989).

[17] A.Yamamoto et al., with help by Toshiba.

[18] J.M.Baze et al., Proceedings of the Intn. Conf. on Magnet Technology, 1987.

[19] A.Yamamoto et al., IEEE Transactions on Magnetics, 24(1988)1421.

[20] We used following parameters in calculation of radiation and interaction thickness:

	X_0	λ_0	λ_0/X_0
aluminum	89 mm	394 mm	4.43
high strength Al alloy	81 mm	380 mm	
copper	14.3 mm	151 mm	
superconductor	16 mm	174 mm	
GFRP	190 mm	530 mm	
CFRP	240 mm	550 mm	

[21] V.Radeka, F.Lobkowicz, private communications.

[22] It is assumed that the pure aluminum of RRR=750 at 4.5 K yields at 4kg/mm^2, while aluminum alloy is linear to above 10kg/mm^2.

[23] A.Yamamoto, private communication.

[24] Y.Asano, Resolution requirements on SSC-muon chamber, contribution paper to the Vancouver workshop on tracking system at the SSC, July, 1989 and JSD-Note-1989-6.

[25] Y.Sakai, Muon (Trigger) rates calculations , JSD-Note-1989-3.

[26] "SSC Muon Detector Group Report", page 405 in Snowmass 1986 Proceedings and A.Bodek, UR911 ER13065-412(1985).

[27] T.Doi et al, status report on a conceptual design study of a hermetic detector for the SSC, JSD-Note-1990-8.

[28] R.Voss and C.Zupancic, ECFA study for LHC, CERN 84-10, p228.

[29] J.J.Eastman ans S.C.Loken, 1987 Berkeley Workshop, p542.

[30] Y.Sakai, private communication.

[31] V.Innocente, 1987 Berkeley Workshop, p.554.

[32] T.Ohsugi & S.Takubo, talk given at the Hadron Collider Physics in Japan, Tohoku U.,May 1988, quoted by S. Sugimotoin the summary talk of the muon group at the Vancouver workshop on tracking system at the SSC, July, 1989.

[33] V.Radeka and S.Rescia, Nucl. Instr. and Methods, A265(1988)228.

[34] T.Adams et al., Presented at the Alabama workshop on calorimetry for the SSC, Tuscaloosa, March 1989.

[35] A.Bay et al., SSC-202.

[36] Y.Fukushima et al., IEEE Trans. on Nucl. Science 36(1989)670.

[37] Study being done by T.Kondo and H.Iwasaki.

[38] M.Gilchriese, Summary talk at the Alabama workshop on calorimetry.

[39] V.Barnes et al., 1987 Berkeley workshop, p235.

[40] J.Brau and T.A.Gabriel, Nucl. Instr. and Methods, A238(1985)489.
R.Wigmans, Nucl. Instr. and Methods, A259(1987)389.
H.Bruckmann, Nucl. Instr. and Methods, A263(1987)136.

[41] Talk on H1 LAr calorimeter at the Alabama workshop,March,1989.

[42] K.Amako and M.Asai, 8th workshop for hadron collider physics in Japan, KEK, July,1989.

[43] K.Ogawa, Effect of e/h ratio on jet energy resolution, JSD-Note-1990-1.

[44] $R=e/h=R_0-(R_0-1)\frac{ln E}{ln 1000}$ for E>1Gev, $R=R_0-R_0\frac{ln E}{ln 0.1}$ for E<1GeV based on M.De Vincenzi et al., CERN-EP/85-126, 1985, where R_0 is the e/f at 1 GeV. In the simulation, energies of e and γ's in the jets were smeared by $s/E=0.15/\sqrt{E}$ while hadrons in the jets were smeared by $A/\sqrt{E}$(A=0.1~1.0) and then were reduced in accordance with the given e/h ratio.

[45] J.Huth, presented at the Alabama workshop on calorimetry, March 1989, Fermlab-Conf-89/117-E.

[46] Report of the Task Force on Detector R&D for the SSC, SSC-SR-1021, June 1986, pp.44-60.

[47] D.G.Cassel & G.G.Hanson, 1986 Snowmass Summer Study, pp.377-387.

[48] J.Kerkby et al., 1987 Berkeley Workshop, 1987, see p.401.

[49] M.Asai, Hit rates of straw chamber tracker, contribution paper to the Vancouver workshop on tracking,1989 and JSD-Note-1990-2.

[50] H.Iwasaki, Talk at the Vancouver Workshop on tracking, July,1989.

[51] J.DeWitt et al., 1988 Snowmass Summer Study, p.717.

[52] T.Ohsugi et al., Nucl. Instr. and Methods, A265 (1988)105.
M.Nakamura et al., Nucl. Instr. and Methods, A270 (1988) 42.

[53] T.Kondo, 1988 Snowmass Summer Study, p.732.
M.Hasegawa et al., Nucl. Instr. and Methods, A277 (1989) 395.
T.Arima et al., Japanese Journal of Applied Physics, 28 (1989) 1957.
T.Ohsugi, talk given at the Alabama workshop on calorimetry, March 1989, HUPD 8903, May 1989.

[54] T.Ohsugi et al., talk given at the Alabama workshop on calorimetry, March 1989, HUPD 8904, May 1989.

[55] T.Ohsugi et al., Report on Radiation Effects at the SSC, June 1988, SSC-SR-1035,p111.

[56] H.Ikeda and N.Ujiie, Nucl. Instr. and Methods, A281 (1989) 508.

H.Ikeda and N.Ujiie, Contribution to the Hadron Collider workshop in Japan, Tsukuba U., Sep. 1989 and submitted to Nucl. Instr. and Methods.

H.F.-W.Sadrozinski et al., Paper presented at ECFA study week on high luminosity hadron colliders, Barcelona, Sep.1989, SCIPP 89/49.

[57] Task Force on Radiation Hardened Electronics at the SSC, June 1988.

[58] H.Ikeda, private communication.

[59] T.Ohsugi and Y.Tajima, contribution to the Vancouver workshop on tracking system at the SSC, July, 1989.

[60] Y.Arai and T.Ohsugi, 1986 Snowmass Summer Study, p.455.

[61] A.Stevens et al., IEEE Trans. Nucl. Sci. NS-36(1988)507.

[62] Y.Arai and T.Ohsugi, KEK Preprint 88-78, Nov. 1988.

[63] Y.Arai, KEK-Preprint 88-130.

[64] T.Ohsugi, M.Asai and Y.Arai, contribution to the Vancouver workshop on tracking system at the SSC, July, 1989 and JSD-Note-1990-3.

[65] Some of material properties of oilless fiber freon are:

tensile strength	> 10kg/mm^2
compress strength	> 20 kg/mm^2
Youngth modulus	> 600 kgf/mm^2
expansion coefficient	2 ~ 3·10^{-5}/°C
conductivity	4 ~ 7·10^{-4} cal/s/°C/cm.

The sliding coefficient of friction is 0.08 ~ 0.09 (static) and 0.03 (dynamic).

[66] T.Ohsugi, Central Tracking Devices for the SSC, JSD-Note-1990-6.